Article

S1PR1-biased activation drives the resolution of endothelial dysfunction-associated inflammatory diseases by maintaining endothelial integrity

Huaping Zheng [1,7], Jingjing Yu[1,2,7], Luhua Gao[1,7], Kexin Wang [1,2,7], Zheng Xu [1,7], Zhen Zeng[3,7], Kun Zheng[1,7], Xiaoju Tang[1,7], Xiaowen Tian[1,2,7], Qing Zhao[1], Jie Zhao [4], Huajing Wan[1], Zhongwei Cao [1], Kang Zhang [5], Jingqiu Cheng[1], Jürgen Brosius [1], Hu Zhang [3], Wei Li[6], Wei Yan [1,4] ✉, Zhenhua Shao [1,2,4] ✉, Fengming Luo[1] ✉ & Cheng Deng [1] ✉

G protein-coupled sphingosine-1-phosphate receptor 1 (S1PR1), a drug target for inflammatory bowel disease (IBD), enables immune cells to egress from lymph nodes, but the treatment increases the risk of immunosuppression. The functional signaling pathway triggered by S1PR1 activation in endothelial cells and its therapeutic application remains unclear. Here, we showed that S1PR1 is highly expressed in endothelial cells of IBD patients and positively correlated with endothelial markers. Gi-biased agonist-SAR247799 activated S1PR1 and reversed pathology in male mouse and organoid IBD models by protecting the integrity of the endothelial barrier without affecting immune cell egress. Cryo-electron microscopy structure of S1PR1-Gi signaling complex bound to SAR247799 with a resolution of 3.47 Å revealed the recognition mode for the biased ligand. With the efficacy of SAR247799 in treating other endothelial dysfunction-associated inflammatory diseases, our study offers mechanistic insights into the Gi-biased S1PR1 agonist and represents a strategy for endothelial dysfunction-associated disease treatment.

In recent years, there has been a growing appreciation for the role of abnormal vessel endothelial barrier, and their immune function involvement have received increasing attention in chronic inflammatory diseases, notably inflammatory bowel disease (IBD)[1,2]. Endothelial cells (ECs), as primary components of blood and lymphatic vessels,
play a crucial role in various physiological processes, including organ regeneration, fibrosis, and cancer development, while also serving as an anti-adhesive and selectively permeable exchange barrier[3–5]. ECs dysfunction impairs barrier integrity, leading to vascular dysplasia, enhanced leukocyte permeability, increased adhesion molecular

[1]Department of Respiratory and Critical Care Medicine, Center for High Altitude Medicine, Institutes for Systems Genetics, State Key Laboratory of Biotherapy, National Clinical Research Center for Geriatrics, West China Hospital, Sichuan University, Chengdu, China. [2]Division of Nephrology and Kidney Research Institute, West China Hospital, Sichuan University, Chengdu, China. [3]Department of Gastroenterology, Lab of Inflammatory Bowel Disease, West China Hospital, Sichuan University, Chengdu, China. [4]Frontiers Medical Center, Tianfu Jincheng Laboratory, Chengdu, China. [5]Center for Biomedicine and Innovations, Faculty of Medicine, Macau University of Science and Technology and University Hospital, Macau, China. [6]Department of Dermatology, Rare Diseases Center, West China Hospital, Sichuan University, Chengdu, China. [7]These authors contributed equally: Huaping Zheng, Jingjing Yu, Luhua Gao, Kexin Wang, Zheng Xu, Zhen Zeng, Kun Zheng, Xiaoju Tang, Xiaowen Tian. ✉e-mail: weiyan2018@scu.edu.cn; zhenhuashao@scu.edu.cn; luofengming@wchscu.cn; dengcheng@wchscu.cn

1

expression, and dysregulated nitric oxide excretion, thus aggravating the inflammatory response in chronic inflammatory disease[1,6-8]. The endothelium expansion observed in IBD angiogenesis is a hallmark of active gut disease and correlates closely to disease severity[9-12]. It is increasingly clear that microvascular ECs play a pivotal role in IBD. A number of drugs exhibiting efficacy in treating IBD have been found to affect the endothelium[10-12], thus calling for treatments that target IBD through the maintenance of ECs' function.

The inflammatory response in chronic inflammatory diseases often damages host tissue and results in organ dysfunction[13-17]. IBD, including ulcerative colitis (UC) and Crohn's disease (CD), manifests as chronic inflammation of the gastrointestinal tract[16] and various immunomodulatory therapies have been developed targeting its inflammatory response, including TNF-α and IL-12/IL-23p40 antibodies, Janus kinase (JAK) inhibitors, and sphingolipid 1 phosphate receptor (S1PR) modulators[18]. Despite the clinical efficacy of these immunotherapies, challenges persist, with remission rates are as low as 20-30% and unresolved complications, such as infections, flu-like symptoms, and heart palpitations[18]. ECs play a crucial role in IBD pathophysiology and are garnering interest for therapeutic targeting in IBD treatment[19-21]. Therefore, the discovery of novel therapeutic strategies for preventing endothelial barrier disruption in IBD is of great importance.

The *S1PR1* gene, encoding a G protein-coupled receptor for the endogenous sphingolipid 1 phosphate (S1P) ligand, recently emerged as a therapeutic target in IBD[22-27]. The S1P-S1PR1 ligand-receptor interaction plays a significant role in lymphocyte egress and chemotaxis, regulating multiple immunologic and cardiovascular effects[28,29], cell proliferation and survival, tumor angiogenesis and metastasis[30,31]. Particularly, the FDA-approved fingolimod and ozanimod, classified as S1PR1 modulators, were proven effective for treating UC by reducing circulating lymphocytes[32,33]. However, these modulators exhibit low specific S1PR1 affinity and potential adverse effects, such as cardiovascular disease, abnormal liver function, and heightened infection risk[34,35]. Recent studies showed that *S1PR1* expression in vascular endothelial cells inhibits angiogenic sprouting and promotes vascular stabilization[36-38], suggesting that targeting S1PR1 in endothelial cells could show promise in treating IBD.

Here, we demonstrated that *S1PR1* is mainly expressed in colonic endothelial cells of IBD patients and a DSS (Dextran Sulfate Sodium) -induced colitis mouse model. We also identified SAR247799, a Gi signaling-biased allosteric modulator of S1PR1, which was highly effective in the therapeutic treatment of colitis in mice. Despite previous assessments on the impact of SAR247799 on macrovascular endothelial function of the brachial artery with flow-mediated dilation (FMD) among type 2 diabetes mellitus (T2DM) patients[39,40], the mechanism of S1PR1 allosteric modulation at the structural level and its function in maintaining endothelial integrity in inflammatory diseases remain elusive. Here, we found SAR247799 primarily influences mainly the endothelial barrier rather than peripheral immune cells. By employing single particle cryo-electron microscopy (cryo-EM), we determine the structure of S1PR1 bound to SAR247799 and its biased Gi signaling. Further, we demonstrated that orally bioavailable Gi-biased S1PR1 agonist SAR247799 ameliorated endothelial dysfunction-associated inflammatory diseases by suppressing vessel permeability and inflammatory cell infiltration.

Results

S1PR1 expression correlates with improved IBD outcomes
To survey *S1PR1* expression levels in patients with IBD, we analyzed publicly available RNA-sequencing (RNA-seq) data generated from intestine biopsies collected from UC or CD patients as well as from healthy individuals (GSE66407, GSE59071). As expected, *S1PR1* mRNA was elevated in both UC and CD patient samples (Fig. 1a and

Supplementary Fig. 1a, b) and positively correlated with endothelial barrier function by measuring the relative expression of human endothelial markers *SELE*, *ITGB1*, *ICAM1*, *ICAM2*, *VCAM1* and *CDH5* (Fig. 1b and Supplementary Fig. 1c, d). We characterized the alterations in S1PR1 during colonic inflammation by following a time course in the DSS-induced colitis mouse model (E-MTAB-9850), showing that *S1pr1* increased during the intestinal inflammation stage and receded at the restoration stage (Fig. 1c), positively correlated with mouse endothelial markers *Sele*, *Pecam1*, *Icam1*, *Icam2*, *Vcam1* and *Cdh5* (Fig. 1d). To identify the cell types expressing S1PR1, we surveyed publicly available single-cell RNA-seq (scRNA-seq) data from healthy and UC samples (GSE114374, GSE231993), as well as scRNA-seq data from a DSS-induced colitis mouse model (GSE148794). Here, we observed that *S1PR1/S1pr1* was mainly expressed by endothelial cells and positively correlated with endothelial markers (Fig. 1e, f and Supplementary Fig. 1e–h). Immunofluorescent (IF) staining showed that the S1PR1 levels were robustly increased in UC patients' colon and co-localized with CD31, a vascular endothelial marker in IBD patients (Fig. 1g), consistent with immunofluorescence staining in the DSS-induced colitis mouse model (Fig. 1h).
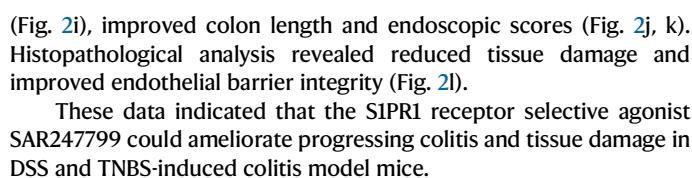
To test the effects of receptor activation in endothelial cells during colitis, we challenged C57BL/6 mice with 2.5% DSS and concomitantly administered S1PR1-selective agonist SAR247799 or IBD therapeutic drugs FTY720 in carboxymethyl cellulose (CMC) solution orally once daily (Fig. 1i). Compared to immunosuppressant FTY720, treatment with 1 mg/kg SAR247799 was most effective in alleviating the progression of colitis with respect to colon length, weight loss, disease activity index (DAI) score, murine endoscopic index of colitis severity (MEICS) score (Fig. 1j–l andSupplementary Figs. 2 and 3a), led to attenuated colonic vascular permeability in colitis mice (Fig. 1m), significantly mitigating tissue damage (Supplementary Fig. 3b)and reduced the infiltration of inflammation cells in colons of colitis mice, without decreasing total leukocyte and lymphocyte percentage (Fig. 1n, o and Supplementary Fig. 4).

Together, these data indicated that *S1PR1*, mainly expressed in the endothelial cells, positively correlated with the degree of IBD disease and endothelial markers, targeting endothelial S1PR1 in the resolution of vascular permeability in IBD.

SAR247799 administration ameliorates colitis in mice
Since our data suggested that the agonist SAR247799 could alleviate the DSS-induced colitis mouse model, we next investigated its therapeutic potential. Mice were treated with 2.5% DSS and monitored for disease onset. Once disease onset was confirmed using fecal blood and diarrhea scores, mice received vehicle only or vehicle with FTY720, ozanimod, 5-ASA or SAR247799 daily for one week (Fig. 2a and Supplementary Fig. 5a). Mice consistently showed rapid recovery from weight loss with 1 mg/kg SAR247799 (Fig. 2b and Supplementary Fig. 5b). In comparison to FTY720, ozanimod and 5-ASA, mice receiving 1 mg/kg SAR247799 showed improved DAI, colon length and endoscopic scores (Fig. 2c–e and Supplementary Fig. 5c, d). Histopathological analysis revealed that SAR247799 treatment reduced tissue damage and improved endothelial barrier integrity and colonic fibrosis (Fig. 2f and Supplementary Fig. 5e, f).

Based on our findings that S1PR1 was expressed at high levels in patients with CD (Fig. 1a), we examined whether SAR247799 also affected a widely used CD mouse model. We induced experimental colitis in mice by intrarectal administration of 2,4,6-trinitrobenzene sulfonic acid (TNBS)[41] (Fig. 2g). Compared to the negative control group, mice treated with TNBS displayed severe body weight loss and colon shortening (Fig. 2h, i). Compared to FTY720, treatment with SAR247799 showed a superior therapeutic effect, almost rescued C57BL/6 mice from weight loss (Fig. 2h) and decreased the DAI score

(Fig. 2i), improved colon length and endoscopic scores (Fig. 2j, k). Histopathological analysis revealed reduced tissue damage and improved endothelial barrier integrity (Fig. 2l).

These data indicated that the S1PR1 receptor selective agonist SAR247799 could ameliorate progressing colitis and tissue damage in DSS and TNBS-induced colitis model mice.

SAR247799 maintains endothelial barrier in colitis mice

To further investigate the SAR247799 mechanisms of action in colitis mice, RNA-seq was performed to evaluate the gene expression profile in DSS-induced colitis tissue after treatment with FTY720, SAR247799, or solvent control, compared with healthy control (Supplementary Fig. 6a). Performing differential expression gene analysis among

Fig. 1 | S1PR1 expression correlates with improved IBD outcomes. a *S1PR1* expression in the IBD gene array expression dataset (GSE66407) from colon biopsies of UC ($n = 101$) and CD ($n = 57$) patients, compared to healthy control (HC, $n = 55$). The definition of the box plots can be found in the 'Methods' section. **b** Correlation between *S1PR1* expression and endothelial markers (left) with statistical analysis (right) in GSE66407. **c** *S1pr1* expression in the E-MTAB-9850 dataset from DSS-induced colitis mice during inflammatory (Inf_mid ($n = 2$), Inf_hi ($n = 3$)) and recovery stages ($n = 3$), compared to HC ($n = 3$). **d** Correlation between *S1pr1* expression and endothelial markers (left) with statistical analysis (right) in dataset E-MTAB-9850. **e** *S1PR1* expression from scRNA-seq analysis of UC ($n = 2$) and HC ($n = 2$) patients colon biopsies, showing cell type-specific clusters (GSE114374). **f** *S1pr1* expression from scRNA-seq analysis of colitis mice colon biopsies cell ($n = 10$), type-specific cluster from dataset GSE148794. **g** immunofluorescence (IF) showing S1PR1 (violet) in ECs of IBD patients, co-staining CD31 (red) and CD3 (green) ($n = 3$). Scale bar, 20 μm. **h** IF showing S1pr1 (violet), in IEC of colitis mice

(arrows) with co-staining CD31(red) and CD3 (green) ($n = 5$). Scale bar, 20 m. **i** Schematic of DSS-induced colitis mouse model treated with SAR247799 (1 mg/kg) or FTY720 (0.3 mg/kg) via intragastric gavage. **j**, Reesentative colon (left), and colon length quantification (right) ($n = 6$). **k** Body weight percentage, and (**l**), disease activity index (DAI) ($n = 6$). **m** Colonoscopy images (top), colon length (left bottom), Evans blue dye leakage from blood vessels (bottom right) after DSS treatment. **n** Blood routine test showing neutrophil, lymphocyte, monocyte, and eosinophil (right) and percentages (left) ($n = 6$). **o** Percentage and counts of CD3+ in CD45+, CD4+ and CD8+ cells in CD3+ populations in PBMCs and LPMCs ($n = 6$). Data are presented as mean ± SEM; Statistical analysis: two-sided Student's *t* test (**a**, **c**, **j**, **m–o**); Spearman's rank correlation analysis (**b**, **d**). Two-way ANOVA with multiple comparisons (**k**, **l**). For (**k**, **l**), the significance of Ctrl+Vehicle vs. DSS + Vehicle is shown as red, DSS + Vehicle vs. DSS + FTY720 or DSS + SAR is shown as cyan and blue *p*-value respectively. All experiments were repeated three times with consistent results.

different treatment groups (Supplementary Fig. 6b), *S1pr1* expression was elevated in the DSS and FTY720 groups but unchanged in the SAR247799 group compared to the control group (Fig. 3a) and the *S1pr1* expression pattern correlated positively with endothelial markers (Fig. 3b). Compared to the FTY720 group and the DSS group, the SAR group exhibits a greater number of downregulated endothelial-related pathways, with its changes being opposite to those observed in the DSS group (Fig. 3c and Supplementary Fig. 6c). Gene Ontology (GO) analysis revealed that the DEG clusters of molecular functions regulated by SAR244779 were related to leukocyte migration and proliferation, and cell-cell adhesion (Supplementary Fig. 6d, e). Kyoto Encyclopedia of Genes and Genomes (KEGG) analysis revealed that the pathways regulated by SAR247799 were cytokine-cytokine receptor interaction, PI3k-Akt signaling pathway, and metabolism (Supplementary Fig. 6f, g). Gene Set Variation Analysis (GSVA) confirmed that SAR247799 group endothelial-related pathways and immune-related pathways are more inclined towards the control group level than the DSS and FTY720 group (Fig. 3d and Supplementary Fig. 6h). The murine Microenvironment Cell Population (mMCP) counter score indicated a similarly decreased infiltration of T cells and CD8+ T cells in the SAR244779 group and the FTY720 group compared to DSS group, while the stromal cell infiltration of SAR244779 group was similar to that of the control group, and the stromal cell infiltration of FTY720 group was similar to that of the DSS group (Fig. 3e). The heatmap of endothelial-related genes showed that the SAR247799 group was similar to control groups, *Pecam1, Vcam1, Cdh5, Sele,* and *Icaml* expression was downregulated compared to DSS and FTY720 groups (Fig. 3f), consistent with qRT-PCR results (Fig. 3g). To further investigate the effects of SAR247799 on endothelial cell-cell interactions, immunofluorescence (IF) staining of Vcam1, CD4 and CD31 was performed, and the results showed that DSS-induced colitis irregular and tortuous vascular network was associated with a loss of Vcam1 and CD31 integrity at cell-cell junctions (Fig. 3h). The SAR247799 group displayed a regular vascular network and less immune cell infiltration (Fig. 3h).

To further confirm that SAR247799 ameliorates colitis primarily by maintaining the endothelial barrier, lymphocytes were assessed by collecting blood, spleen, and mesenteric lymph nodes from WT mice administered with varying concentrations of SAR247799. Unlike FTY720, which significantly reduced CD3+ T cells in CD45+ immune cells and altered the proportion of CD4+ and CD8+ T cells in peripheral blood, SAR247799 showed no effect on lymphocyte populations. (Supplementary Fig. 7). *Rag2-/-* mice were performed DSS induced colitis to investigate the therapeutic effects of SAR247799 in the absence of T cells (Supplementary Fig. 8a). Compared to FTY720, treatment with SAR247799 showed a superior therapeutic effect, attenuated weight loss and DAI scores (Supplementary Fig. 8b, c), improved colon length (Supplementary Fig. 8d). Histopathological and colonoscopy analysis revealed reduced tissue damage (Supplementary

Fig. 8e, f) and improved endothelial barrier integrity independent with CD3+ T cells (Supplementary Fig. 8g). In addition, CD4+ CD25- T cell transfer colitis model (Supplementary Fig. 9a) showed SAR247799 treatment significantly ameliorates weight loss, DAI scores, colon length, histopathological damage and colonoscopy scores (Supplementary Fig. 9b–f). The homing of T cells to the spleen and intestinal lymph nodes was not affected (Supplementary Fig. 9g).

Our results showed that SAR247799 primarily mediates the endothelial barrier to counteract progressing colitis and tissue damage in colitis mouse models by maintaining the endothelial barrier.

SAR247799 protects the endothelial barrier in human colon crypts and human umbilical vein endothelial cells (HUVEC)

Our previous in vivo results indicated that SAR247799 protects the endothelial barrier by maintaining the integrity of the endothelial cell connection (Fig. 3). To further understand the effects of SAR247799 treatment, we purified human colon crypts from tissue samples obtained from colectomies or biopsies from IBD patient tissue. Crypt fragments were cultured in a three-dimensional matrigel matrix for 10–12 days (Supplementary Fig. 10a). We monitored Icam1, Vcam1, E-selectin, and CD31 expression in the colon crypts induced by TNF-α with SAR247799 and FTY720. The result showed that SAR247799 significantly reduced the expression of adhesion molecules in human colon crypts (Fig. 4a). GSVA results of RNA-seq data suggested that the endothelial and immune-related pathways' GSVA score of SAR247799 treated TNF-α induced crypts was similar to blank crypts (Fig. 4b–d). The KEGG and GOBP showed that SAR247799 treatment significantly affected the cAMP signaling pathway, cell adhesion molecules, and Th1 and Th2 cell differentiation (Fig. 4e, f and Supplementary Fig. 10b, c).

To ascertain the effect of SAR247799 on the endothelial cells, we constructed S1PR1 knockdown HUVEC cell lines (Fig. 4g). The qRT-PCR results indicated that SAR247799 had no effect on the expression of endothelial related genes, *ICAM1*, *VCAM1* and *SELE* in S1PR1 knockdown HUVEC (Fig. 4h).

Taken together, SAR247799 activating S1PR1 affected the expression of tight binding and adhesion molecules on endothelial cells, thereby recuperating the integrity of the endothelial barrier and alleviating the occurrence and development of IBD.

Pharmacological investigation of SAR247799 and overall structure of SAR247799 bound S1PR1-Gi complex

S1PR1 engages distinct cellular signaling pathways, including the Gi and the β-arrestin pathways, when sensing extracellular stimuli. Unlike endogenous ligand S1P, current drugs, such as FTY720 and siponimod, activate S1PR1 and induce sustained internalization of S1PR1 through its β-arrestin signaling pathway, which prevents the migration of lymphocytes in the treatment of multiple sclerosis[42]. Recent studies have shown that SAR247799 barely induces S1PR1 internalization[39], suggesting a weak β-arrestin signaling effect of SAR247799. This
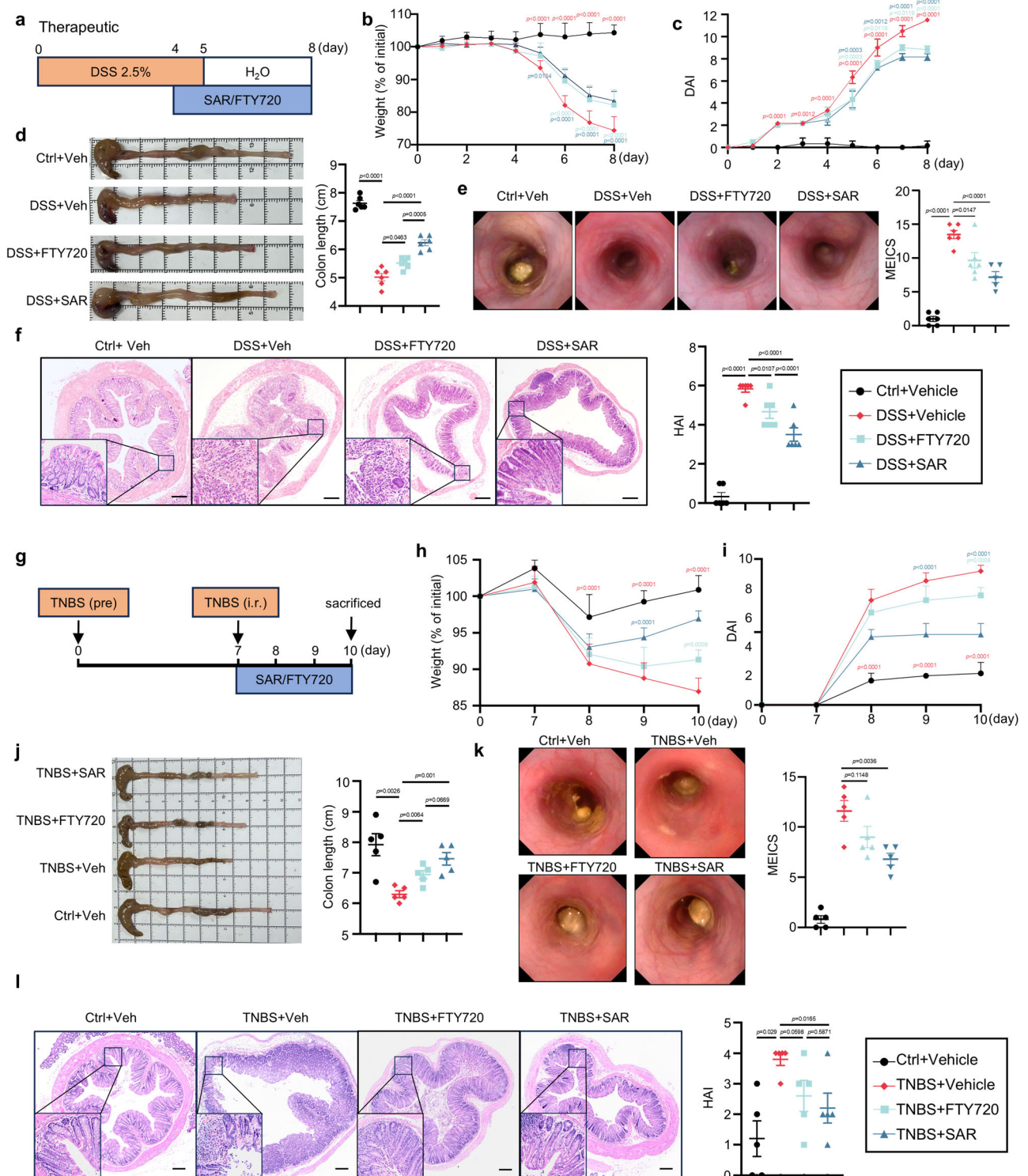
Fig. 2 | SAR247799 administration ameliorates colitis in mice. a Schematic representation of DSS-induced colitis mouse model with SAR247799 (1 mg/kg) and FTY720 (0.3 mg/kg) treatments (intragastric gavage, i.g.). **b, c** Body weight percentage and disease activity index (DAI) (*n* = 6). **d** Representative images of colon (left) and quantification of colon length (right) (*n* = 6). **e** Representative colonoscopy images (left) and MEICS scores (right) (*n* = 6). **f** Representative images of H&E (left) and histological activity index (HAI) analysis (right). Scale bar, 200 μm (*n* = 6). **g** Schematic representation of TNBS-induced mouse colitis with SAR247799 (SAR, 1 mg/kg) and FTY720 (0.3 mg/kg) treatments (intragastric gavage, i.g.). **h, i** Body weight percentage and disease activity index (DAI) (*n* = 5). **j** Representative images of colon (left) and quantification of colon length (right) (*n* = 5). **k** Representative

coloscopy images (left) and MEICS scoring (right) (*n* = 5). **l** Representative images of H&E (left) and HAI analysis (right). Scale bar, 200 μM (*n* = 5). Data are presented as mean ± SEM; Statistical analysis: two-sided Student's *t* test (**d**–**f**, **j**–**l**), Two-way ANOVA with multiple comparisons (**b**, **c**, **h**, **i**). For (**b** and **c**), the significance of Ctrl +Vehicle versus DSS + Vehicle was shown as red, DSS + Vehicle versus DSS + FTY720 or DSS + SAR was shown as cyan and blue *p*-value respectively; For (**h** and **i**), the significance of Crtl + Vehicle versus TNBS + Vehicle was shown as red, TNBS + Vehicle versus TNBS + FTY720 or TNBS + SAR was shown as cyan and blue *p*-value respectively. All biological experiments were repeated three times and yielded consistent results.

6
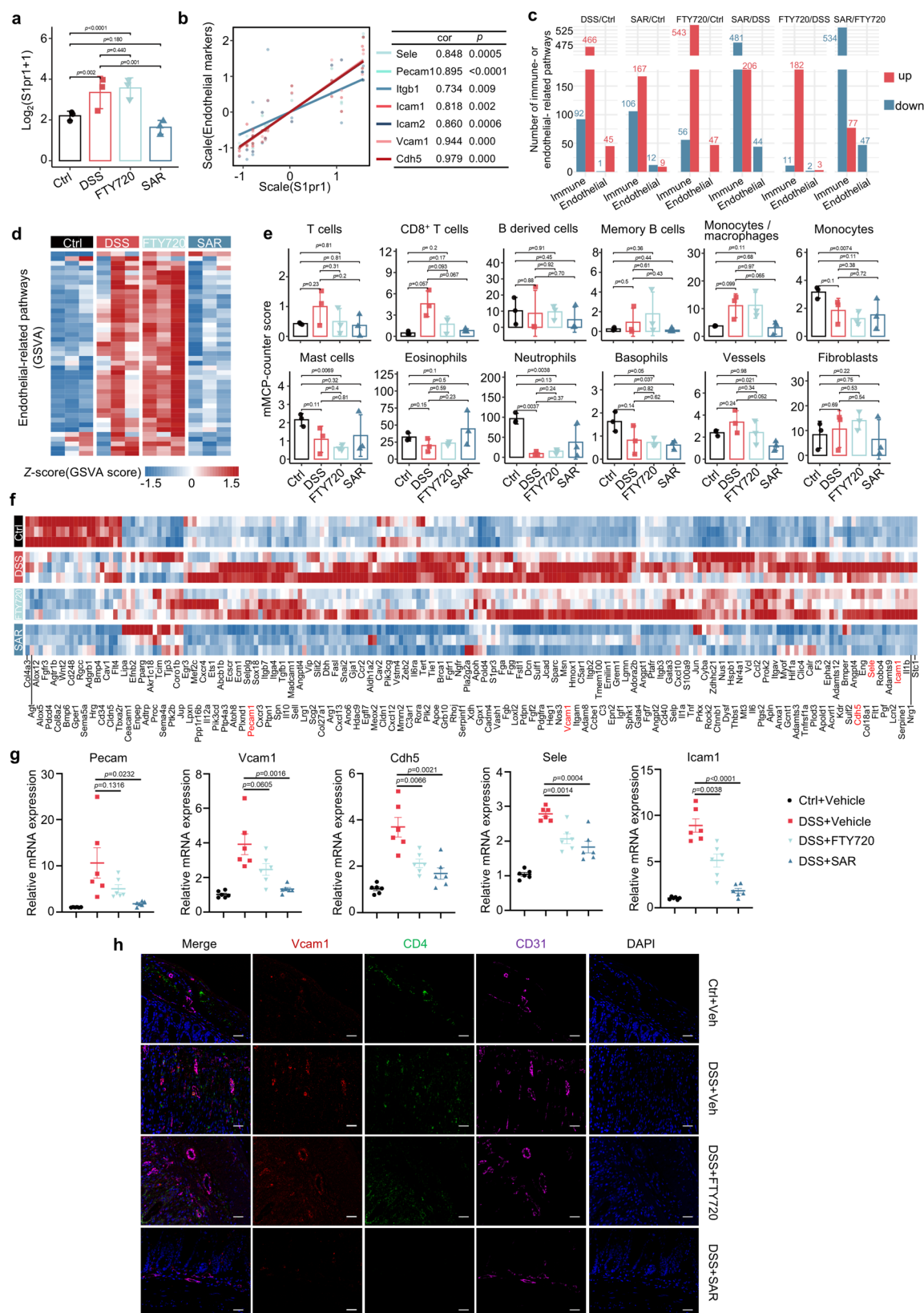
particular signaling bias may be related to its ability to exert a therapeutic effect on IBD, yet the molecular mechanism of this biased activation is unclear.

To characterize the pharmacological features of SAR247799, we conducted G protein dissociation and bioluminescence resonance energy transfer (BRET)-based β-arrestin2 recruitment assays on *S1PR1*

expressing CHO cells, respectively. Compared to fingolimod-phosphate (FTY720-P), SAR247799 induced a comparable activation of Gi1 signaling, but had a weaker ability of β-arrestin2 recruitment (Fig. 5a, b and Supplementary Tables 1 and 2), which indicates that SAR247799 exhibited a Gi-biased agonist for S1PR1 relative to FTY720-P (Fig. 5c).

Fig. 3 | SAR247799 maintains endothelial barrier in colitis mice. a mRNA expression of *S1pr1* in colon of DSS-induced colitis mouse with SAR247799 and FTY720 treatments, Ctrl: Ctrl + Vehicle (*n* = 3), DSS: DSS + Vehicle (*n* = 3), FTY720: DSS + FTY720 (*n* = 3), SAR: DSS + SAR247799 (*n* = 3). **b** mRNA expression of endothelial markers shows a positive correlation (Spearman) with *S1pr1* expression (*n* = 3). **c** Summary of the count of immune- and endothelial-related pathways in all pairwise comparisons of GOBP enrichment results. **d** Heatmap illustrating GSVA scores for pathways related to endothelial functions (*n* = 3). **e** mMCP scores for the four groups (*n* = 3). **f** Heatmap of genes involved in endothelial-related pathways identified through GOBP enrichment analysis (*n* = 3). **g** mRNA level of *Pecam*, *Vcam1*, *Cdh5*, *Sele* and *Icam1*, (*n* = 6). **h** Representative IF for Vcam1(red), CD3 (green) and CD31 (violet) colon of colitis mice(*n* = 6). Scale bar, 50 μm. Data are presented as mean ± SEM; Statistical analysis: two-sided Student's *t* test (**a**, **e**, **g**) and Spearman's rank correlation analysis (**b**). All biological experiments were repeated three times and yielded consistent results. Source data are provided as a Source Data file.

SAR247799 has a significantly different chemical skeleton compared to FTY720-P. The mechanism of how it interacts with the receptor to mediate Gi1-biased activation is poorly characterized. To elucidate this question, we solved the structure of the SAR247799-bound S1PR1-Gi1 complex with a resolution of 3.47 Å by single-particle cryo-EM technique (Fig. 5d, Supplementary Fig. 11a–c and Supplementary Table 3). The overall architecture is similar to that of other resolved S1PR1-Gi complexes. Still, the densities of the N-terminus of S1PR1, as well as the N-termini of Gβ and Gγ, are not clear (Fig. 5d and Supplementary Fig. 11d). The ligand has a pronounced continuous density within the transmembrane (TM) helices core and was unambiguously modeled in the orthosteric binding pocket of S1PR1 (Fig. 5d). We also further confirmed the stability of SAR247799 in this binding pose by the results of the molecular dynamic (MD) in duplicate (Supplementary Fig. 11e). As observed with class A family GPCRs[43–46], the significant hallmark of the structural feature of S1PR1 activated by SAR247799 is the outward movement of TM6 (Supplementary Fig. 11f).

Mechanisms of SAR247799 in S1PR1

In the complex structure, the SAR247799 molecule occupies the orthosteric binding pocket (OBP) (Fig. 6a). The acetic acid and 2,6-dimethylphenoxy moieties of SAR247799 are embedded in the outer pocket formed among TM3, TM7, ECL1, and ECL2; the oxazolo-pyrimidin moiety is sandwiched by TM3 and TM6, and the remaining chlorophenoxy moiety penetrates deep into the interior of the pocket, between TM3 and TM7 (Fig.6a and Supplementary Fig. 12a). Although the overall configuration of SAR247799 is similar to that of FTYP720-P[47,48], the chemical backbone of SAR247799 within the pocket, unlike the long hydrophobic alkane chain of FTY720-P, contains aromatic and polar moieties, which may play different roles in activation of S1PR1 (Fig. 6b).

To systematically assess how SAR247799 and FTY720-P differ in their interactions with S1PR1, we used Protein Atlas Contact[49] to calculate and evaluate residues on S1PR1, which potentially interact non-covalently with SAR247799 and FTY720-P, respectively (Fig. 6c and Supplementary Fig. 12b). We found nine residues (referred core-residues, hereafter) in contact with both ligands that mainly clustered near the center of the ligands (Fig. 6c, d). Moreover, eight residues interacted with SAR247799, and five residues acted only with FTY720-P, mostly localized on either side of the ligands (Fig. 6c and Supplementary Fig. 12c). These different action modes between FTY720-P and SAR247799 on S1PR1 may provide insights into understanding the biased mechanism of S1PR1 action. Combined with alanine substitution and signal transduction experiments (Supplementary Fig. 13 and Supplementary Tables 1 and 2), we found that core-residues R120$^{3.28}$A and E121$^{3.29}$A, which significantly abolished the agonism of FTY720-P, but moderately affected upon SAR247799 activation (Fig. 6f and Supplementary Tables 1 and 2). In addition, L128$^{3.36}$A and L272$^{6.51}$A mutants completely abolish SAR247799 and FTY720-P induced β-arrestin2 recruitment, with relatively small or moderate effects on the Gi protein pathway (Supplementary Fig. 12e, Supplementary Table 1 and 2). At the same time, our data suggest that a mutant of M124$^{3.32}$A may affect expression, and we attempted to increase the cell surface expression levels of this mutant consistent with WT, but the effect was not significant. Moreover, mutation of the five contact residues only with FTY720-P reduced both Gi dissociation and β-

arrestin2 recruitment stimulated by FTY720-P but had no or little effect on SAR247799 (Supplementary Fig. 13b, c and Supplementary Tables 1 and 2). In addition, for the residues specifically in contact with SAR247799, we found that three mutants S129$^{3.37}$A, V194^{ECL2}A, and L174$^{4.56}$A, significantly reduced the Gi signaling efficacy but slightly reduced or enhanced the β-arrestin2 recruitment-induced by SAR247799, indicating the β-arrestin2 biased characteristics of these mutants relative to wild-type S1PR1 (Fig. 6g, Supplementary Fig. 12d and Supplementary Table 1). When activated by FTY720-P, the three mutants showed un-biased effects on G protein and β-arrestin2 signaling (Fig. 6g, Supplementary Fig. 12d, and Supplementary Table 2). Meanwhile, we also found that the L297$^{7.39}$A mutant significantly affected SAR247799 and FTY720-P induced β-arrestin2 recruitment signaling of S1PR1, yet slightly influenced Gi protein signaling (Supplementary Fig. 12e and Supplementary Tables 1 and 2).

These results revealed that the interactions between S129$^{3.37}$, V194^{ECL2}, and L174$^{4.56}$ of S1PR1 and SAR247799 are essential for the SAR247799-activated Gi-biased signaling of S1PR1. And combined with previous studies[48], we hypothesized that the network of hydrophobic interactions between residues L128$^{3.36}$, L272$^{6.51}$, and L297$^{7.39}$ in the S1PR1 binding pocket is important for SAR247799 and FTY720-P transmitting β-arrestin2 signaling to the PIF and NPxxY motifs (Supplementary Fig. 12f).

## Biased SAR247799 S1PR1-Gi activation is essential for endothelial barrier therapy

To further validate the Gi-biased activation of S1PR1, crucial for elucidating the role of SAR247799 in maintaining the vascular endothelial barrier, Gi inhibitor pertussis toxin (PTX) conditional knock-in mice (*Tox1* cKI) were established (Supplementary Fig. 14a, b). The effect of SAR247799 depended on Gi signaling, as evidenced by the phenotype of the *Tox1^{ΔCdh5}* mice, SAR247799 treatment countered weight loss (Fig. 7a), reduced the DAI score (Fig. 7b), improved colon length (Fig. 7c), lowered endoscopic scores (Fig. 7d), and diminished histopathological damage (Fig. 7e) in DSS-induced colitis of *Tox1^{ΔCdh5}* mice. Meanwhile, colonic vascular permeability improvement was decreased (Fig. 7f).

In addition, *Arrb2^{ΔCdh5}* mice were generated to monitor S1PR1 b-arrestin signaling on the endothelial barrier function during SAR247799 therapy for IBD (Supplementary Fig. 14c, d). The results showed that S1PR1 β-arrestin signaling was not involved in SAR247799 alleviating DSS-induced colitis. SAR247799 treatment maintained the improvement of weight loss (Fig. 7a), the DAI score (Fig. 7b), colon length (Fig. 7c), endoscopic scores (Fig. 7d), histopathological damage (Fig. 7e) and colonic vascular permeability (Fig. 7f) in DSS-induced colitis of *Arrb2^{ΔCdh5}* mice, compared to DSS-induced colitis of *Arrb2$^{f/f}$* mice.

These results showed that Gi signaling of S1PR1 is essential for SAR247799-mediated endothelial barrier maintenance, alleviating DSS-induced colitis.

SAR247799 treatment has a protective effect in inflammatory lung disease mouse model

Endothelial injury and the ensuing vascular permeability are problematic consequences of the response to idiopathic
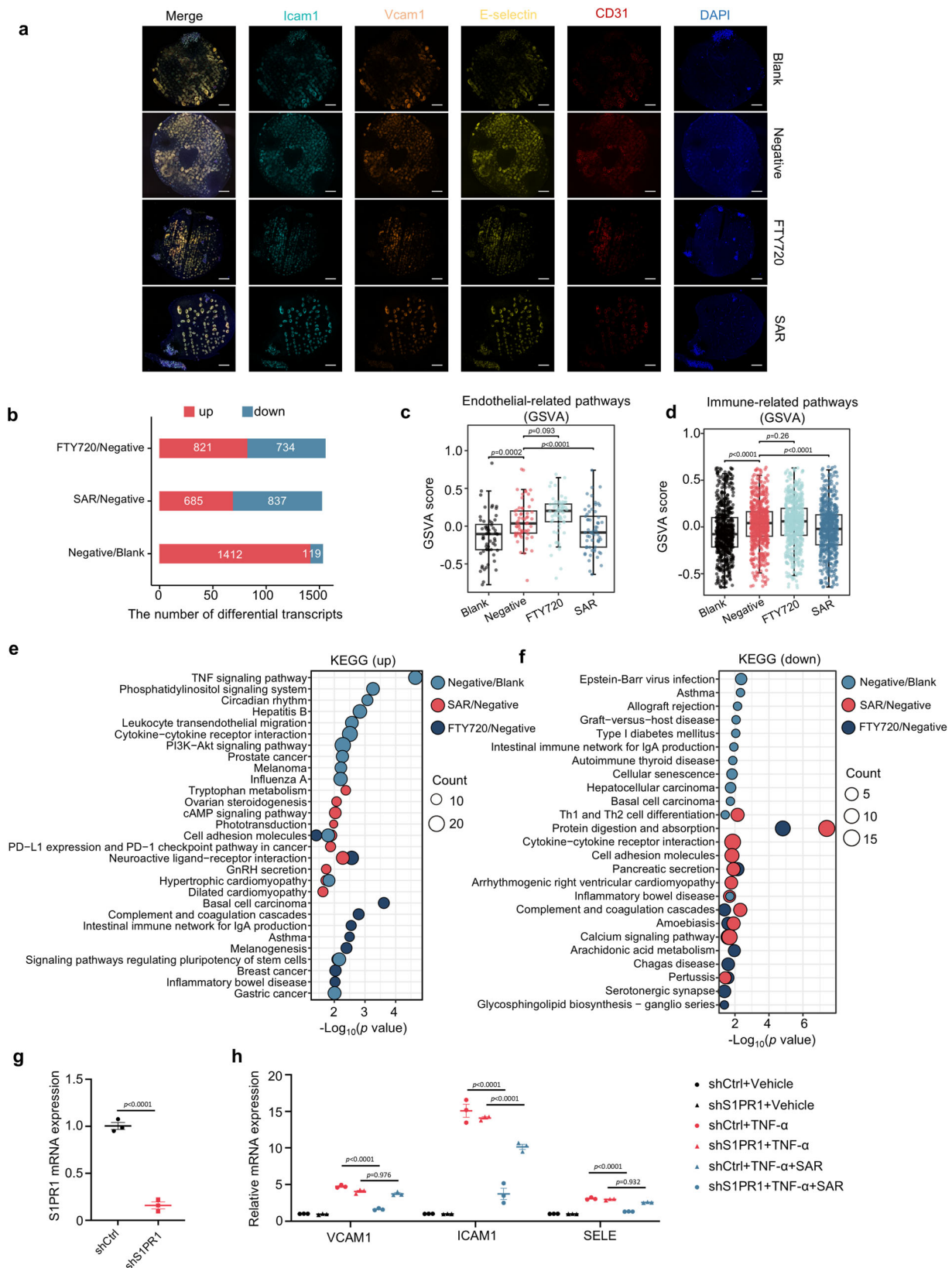
pulmonary fibrosis (IPF) and chronic obstructive pulmonary disease (COPD) tissue injury[50,51]. We analyzed public databases and found that S1PR1 was highly expressed in IPF (Supplementary Fig. 15a, b) and COPD (Supplementary Fig. 15c) patient's lung endothelial cells. To test whether SAR247799 treatment had a protective effect in mouse models of IPF and COPD, we

administered 3.0 mg/kg bleomycin intratracheally to induce lung injury, based on intratracheal administration of bleomycin as the most widely used model of pulmonary fibrosis in mice[52] (Fig. 8a). SAR247799 treatment significantly alleviated bleomycin-induced weight loss (Fig. 8b), down-regulated the mRNA levels of fibrosis markers (Fig. 8c), and markedly decreased the content of

Fig. 4 | SAR247799 protects the endothelial barrier in human colon crypts and human umbilical vein endothelial cells (HUVEC). a Representation IF staining Icam (cyan), Vcam1 (orange), E-selectin (light yellow) CD31 (red) of induced human ulcerative colitis organoid (iHUCO) generation protocol followed by TNF-α administration (Negative group) with SAR247799 (SAR group) and FTY720 (FTY720 group) treatment ($n = 3$); Scale bar, 200 μM. **b** Summary of the count of DEGs identified in all pairwise comparisons of differential expression analysis using Gfold with RNA-seq data, with each group containing one sample. **c**, **d** Box-plot illustrating GSVA scores for pathways related to endothelial functions or related to immune. Each point represents the GSVA score of a pathway. The definition of the

box plots can be found in the 'Methods' section. **e**, **f** The KEGG enrichment results. The figures depict pathways that ranked among the top 10 in at least one set of pairwise comparisons. **g**, qRT-PCR analysis of *S1PR1* expression levels in HUVEC cells after transfection with *S1PR1* shRNA and overexpression *S1PR1* plasmid ($n = 3$). **h** RT-PCR analysis of endothelial and chemokine markers in knockdown and overexpression S1PR1 HUVEC cells ($n = 3$). Data are presented as mean ± SEM; Statistical analysis: GFOLD (**b**), two-sided Student's t test (**c** and **d**, **g**, and **h**), and Hypergeometric Test (**e** and **f**). All biological experiments were repeated three times and yielded consistent results. Source data are provided as a Source Data file.
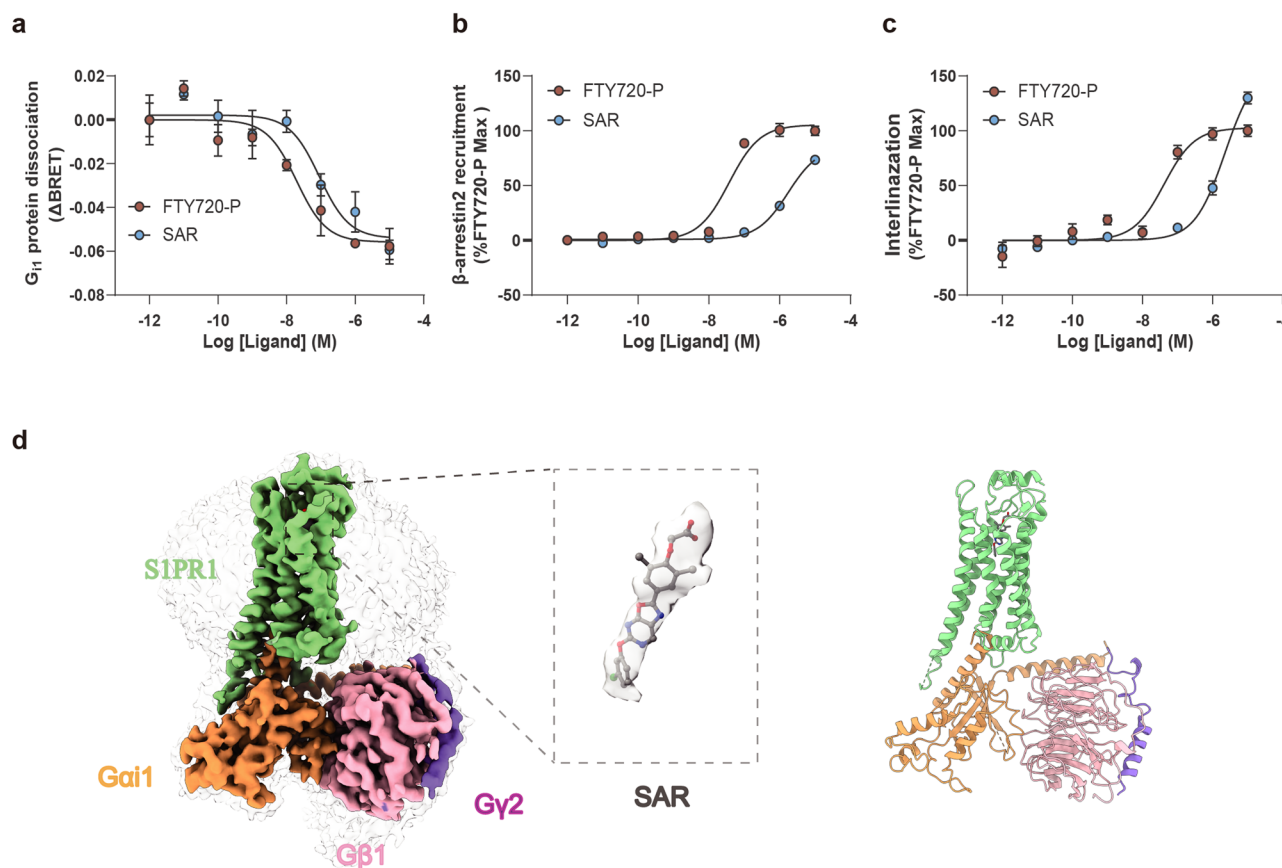

Fig. 5 | Pharmacological features and structural characterization of S1PR1 protein with Gi protein. a, **b** Concentration-dependent response curves of S1PR1 in response to ligands by Gαi -Gγ dissociation assay and β-arrestin recruitment. Data represent mean ± SEM from three independent experiments. **c** Internalization of S1PR1 in CHO cells treated with SAR247799 and FTY720-P. Data represent
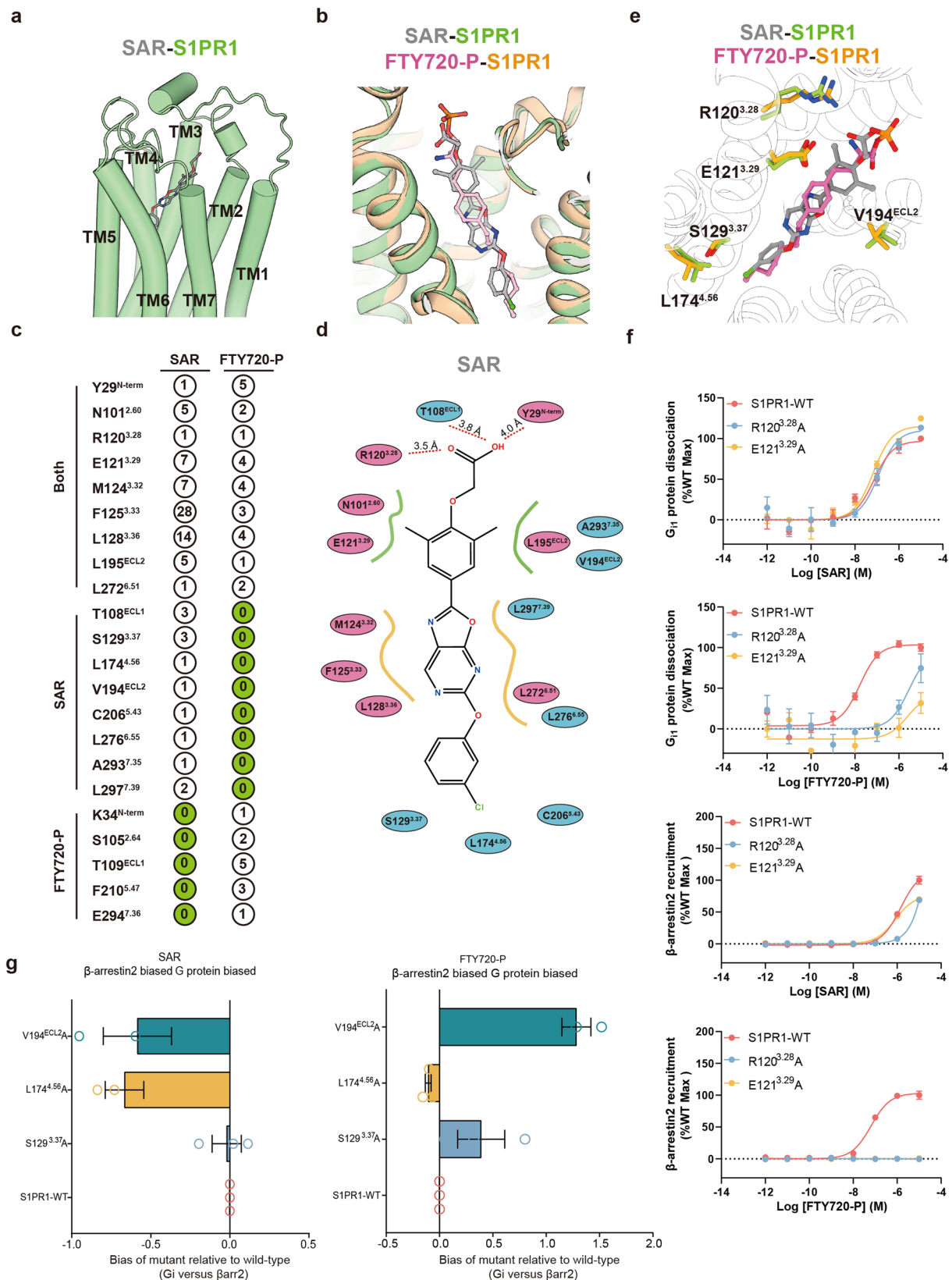
mean ± SEM from three independent experiments. **d** Overview of the cryo-EM density (left) of the S1PR1-Gi complex with SAR247799 and the model (right) of the complex structure. Light green, S1PR1; gray, SAR247799; sandy brown, Gαi1; light pink, Gβ; medium purple, Gγ.

hydroxyproline (HYP) (Fig. 8d). Histology of the lungs at day 14 demonstrated increased fibrosis by H&E staining, and increased collagen deposition, as shown by Masson's trichrome staining (Fig. 8e, f). The COPD-like chronic pulmonary inflammation model was generated by porcine pancreatic elastase (PPE) combined with low-dose lipopolysaccharide (LPS) to investigate the therapeutic effects of SAR247799 (Fig. 8g). The results showed that SAR247799 could effectively alleviate the weight loss caused by the disease model (Fig. 8h), and H&E staining showed a significant reduction in disease severity (Fig. 8i). Periodic acid-Schiff staining showed that SAR247799 treatment markedly decreased polysaccharide production (Fig. 8j).

These results implied that SAR247799 has great promise for the treatment of chronic inflammatory endothelial-dysfunction-associated lung diseases.

Discussion

In recent decades, nonsteroidal anti-inflammatory drugs (NSAIDs) have been the first choice for the treatment of clinical pathologies, including pain inflammatory disease, as well as cancer prevention and treatment[53]. Despite the prevalent use, NSAIDs have been associated with several severe side effects, including gastrointestinal tract toxicity, acute kidney injury, hypertension, and cardiovascular effects[54]. Concurrently, immunotherapy stands out as a primary therapeutic modality in oncology and other autoimmune diseases[55–57], but such treatment benefits are not applicable to the majority of patients[58–60]. Certain immunotherapy approaches like IL-2 and immunotoxin therapies carry the risk of vascular leak syndrome (VLS), leading to increased vascular permeability and potentially complications such as interstitial edema and organ failure[61]. Notably, endothelial dysfunction is a potential contributing factor in the etiology of IBD and other inflammatory-

a SAR-S1PR1

b SAR-S1PR1 FTY720-P-S1PR1

e SAR-S1PR1 FTY720-P-S1PR1

c

		SAR	FTY720-P
Both	$Y29^{N-term}$	1	5
	$N101^{2.60}$	5	2
	$R120^{3.28}$	1	1
	$E121^{3.29}$	7	4
	$M124^{3.32}$	7	4
	$F125^{3.33}$	28	3
	$L128^{3.36}$	14	4
	$L195^{ECL2}$	5	1
	$L272^{6.51}$	1	2
SAR	$T108^{ECL1}$	3	0
	$S129^{3.37}$	3	0
	$L174^{4.56}$	1	0
	$V194^{ECL2}$	1	0
	$C206^{5.43}$	1	0
	$L276^{6.55}$	1	0
	$A293^{7.35}$	1	0
	$L297^{7.39}$	2	0
FTY720-P	$K34^{N-term}$	0	1
	$S105^{2.64}$	0	2
	$T109^{ECL1}$	0	5
	$F210^{5.47}$	0	3
	$E294^{7.36}$	0	1

d SAR

f

g SAR β-arrestin2 biased G protein biased

FTY720-P β-arrestin2 biased G protein biased

related diseases[62]. During the inflammatory process, functional and structural alterations occur within the vascular endothelium[63], characterized by increased leukocyte adhesiveness, diapedesis, heightened vascular smooth muscle tone, and procoagulant activity[63]. In addition, the excessive accumulation of extracellular matrix components in the intestinal wall was characterized in IBD, leading to thickening and scarring[64–66]. More research efforts are directed towards understanding the role of endothelial cells in inflammatory diseases and as potential therapeutic target[6,67–69]. The application of endothelial cell adhesion molecule E-selectin inhibitor demonstrated effectiveness in improving acute myeloid leukemia therapy by disrupting vascular niche-mediated pro-survival signaling[70], and the therapeutic effects of anti-ICAM1

Fig. 6 | Structural basis of signal bias in S1PR1. a The orthosteric binding pocket of SAR247799 in S1PR1. SAR247799 is shown in. Gray. **b** Superposition of SAR247799 and FTY720-P binding modes. **c** Residue distribution by functional relevance and its impact on efficacy and potency. The ligands contact with residues of S1PR1 within 4.2 Å. Polar interactions are highlighted as red dashed lines. **d** Schematic of interactions between SAR247799 and S1PR1. Residues contacting with both SAR247799 and FTY720-P are shown in pink ovals, and only with SAR247799 are displayed in blue ovals. **e** Key residues are shown in sticks and colored in light green (SAR247799-bound S1PR1) and orange (FTY720-P-bound S1PR1). **f** Representative curve for effects of the S1PR1 R120$^{3.28}$ and E121$^{3.29}$ mutations on SAR247799 and FTY720g-P induced G$_{\alpha i1}$-G$_{\gamma 2}$ dissociation assay and β-arrestin2 recruitment in CHO cells. Data represent mean ± SEM from three independent experiments. **g** Bias factors of representation residues in S1PR1 relative to wild-type induced by SAR247799 and FTY720-P. Data represent mean ± SEM from three independent experiments. All biological experiments were repeated three times and yielded consistent results.
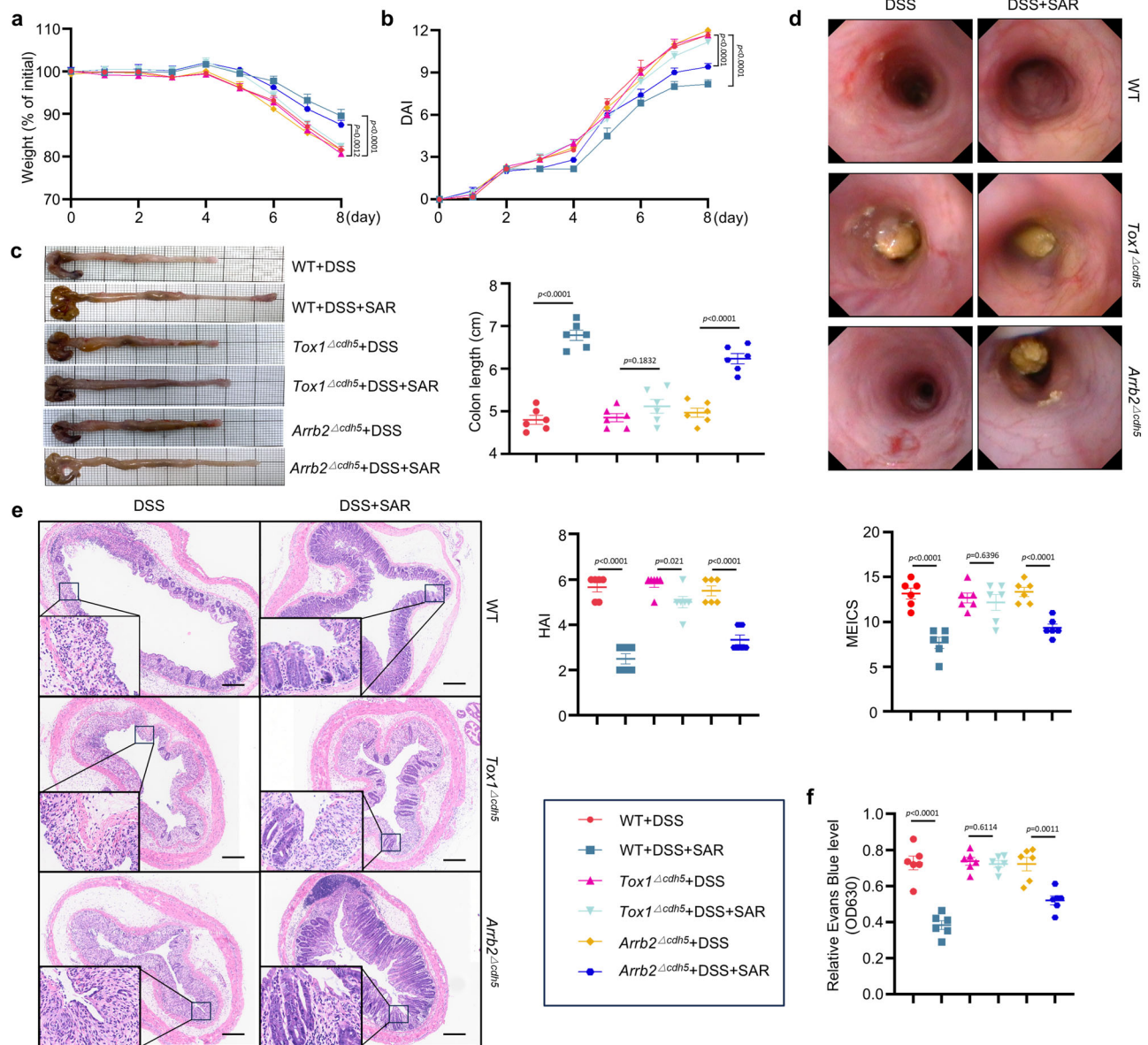
Fig. 7 | Biased SAR247799 S1PR1-Gi activation is essential for endothelial barrier therapy. a DSS-induced *Tox1$^{\Delta Cdh5}$* mice and *Arrb2$^{\Delta Cdh5}$* mice colitis with SAR247799 (1 mg/kg) and FTY720 (0.3 mg/kg) treatments (intragastric gavage, i.g.) body weight percentage (*n* = 6). **b** disease activity index (*n* = 6). **c** Representative images of colon (left) and quantification of colon length (right) (*n* = 6). **d** Representative coloscopy images (top) and MEICS scores (bottom). **e** Representative images of H&E (left) and HAI analysis (right) (*n* = 6). **f** Quantification of Evans blue dye leakage from blood vessels (*n* = 6). Data are presented as mean ± SEM; Statistical analysis: Two-way ANOVA with multiple comparisons (**a, b**), two-sided Student's *t* test (**c–f**). All biological experiments were repeated three times and yielded consistent results.

antibodies in relapsing colitis have been assessed in several experimental models with mixed results[71]. Vedolizumab blocks the α4β7 integrin, which recognizes *MAdCAM-1* expressed on the endothelial in the lamina propria of the gut, reducing the Mayo Clinic score and maintaining clinical remission[72].

GPCRs are targeted by about a third of all therapeutic drugs, with cell communication through heterotrimeric G protein signaling and arrestin binding. Biased agonizts in GPCR drug discovery, such as a μ-opioid receptor, AT1R, β2AR, and TGR5[73–80], have garnered great interest due to their potential to produce safer drugs[81]. S1PR1, a classic
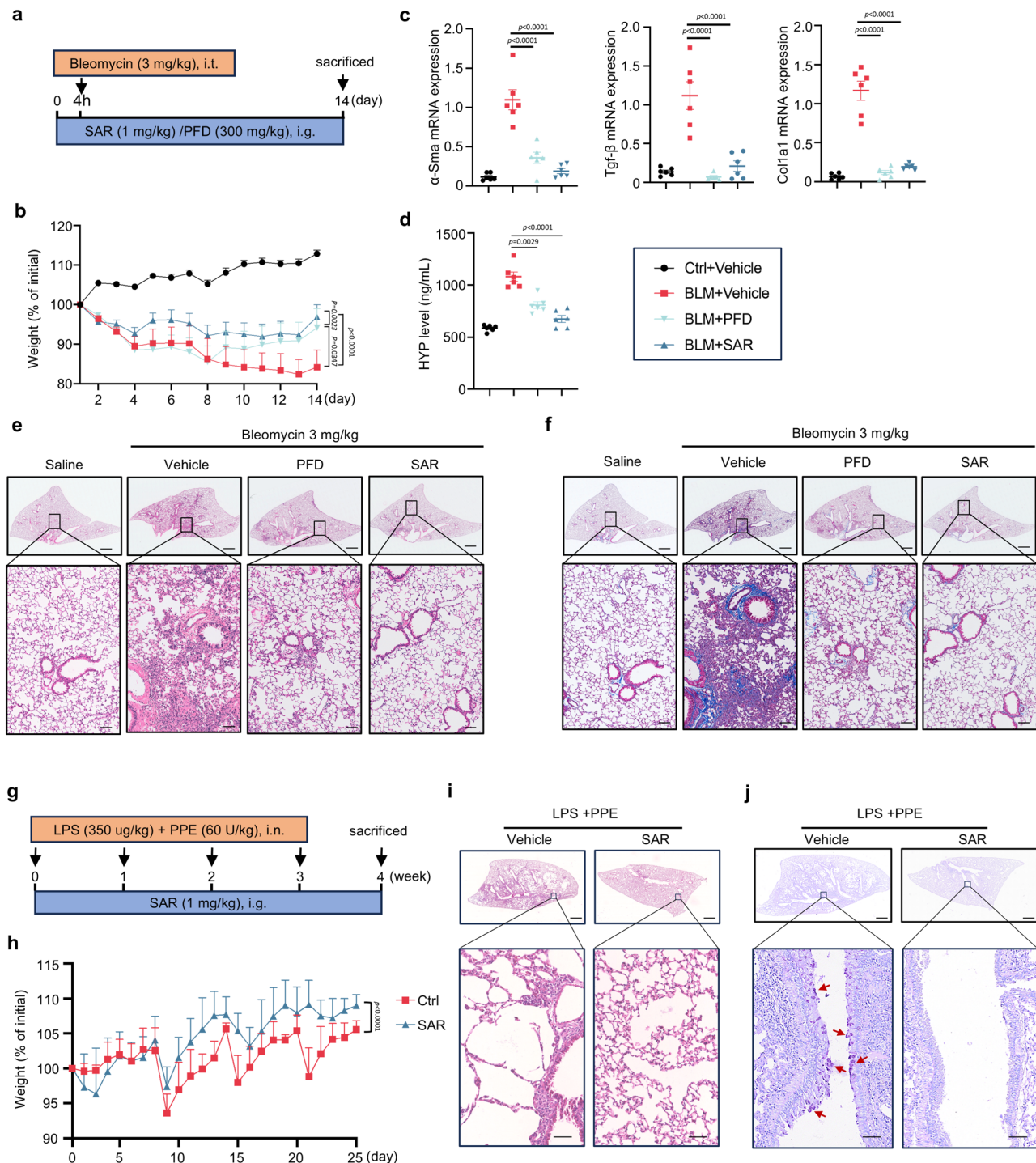
Fig. 8 | SAR247799 protects the endothelial barrier in a lung fibrosis mouse model. a Schematic representation of bleomycin-induced mouse fibrosis model with SAR247799 (1 mg/kg) and pirfenidone (300 mg/kg) treatments (intragastric gavage, i.g.). **b** Body weigh percentage ($n = 6$). **c** mRNA level of fibrosis markers *α-Sma*, *Tgf-β,* and *Col1a1* ($n = 6$). **d** hydroxyproline level in lung tissues ($n = 6$). **e** Representative images of H&E ($n = 6$). Scale bar, 2 μm (above),100 μm (below). **f** Masson's trichrome staining representative images ($n = 6$), Scale bar, 2 μm (above),100 μm (below). **g** Schematic representation of LPS and PPE-induced mouse COPD-like model with SAR247799 (1 mg/kg) treatments (intragastric gavage, i.g.). **h** Body weigh percentage. **i** Representative images of H&E staining ($n = 6$). Scale bar, 2 μm (above),100 μm (below). **j** Representative images of Periodic acid-Schiff staining ($n = 6$). Data are presented as mean ± SEM; Statistical analysis: Two-way ANOVA with multiple comparisons (**b**, **h**), two-sided Student's *t* test (**c**, **d**). All biological experiments were repeated three times and yielded consistent results.

GPCR ubiquitous in the immune, epithelial, tumor, and mesenchymal stromal cells, acts as a regulator of lymphocyte trafficking[82,83]. Deficiency of S1PR1 remarkably decreases circulating lymphocytes[84,85]. An intrinsic requirement for S1PR1 was established by adoptive cell transfer experiments in mice, showcasing its distinctive roles in the egress of T and B cells from lymphoid organs and facilitating the entry of these cells into secondary lymphoid organs[86–88]. Previous studies mentioned that S1PR1 signaling regulates blood flow and pressure and that S1PR1⁺ endothelial cells promote the restoration of vascular integrity[38,89,90]. Here, we found that *S1PR1* is highly expressed in

endothelial cells and positively correlated with the expression of endothelial markers (Fig.1). Moreover, Gi-biased agonist SAR247799, upon activation of S1PR1, reversed the pathology in both mouse and organoid IBD models, by protecting the integrity of the endothelial barrier without perturbing immune cell egress (Figs. 1–4). Furthermore, we determined a cryo-EM structure of SAR247799-bound S1PR1 in the complex at a resolution of 3.4 Å (Fig. 5). We showed that the agonist FTY720-P binds to the receptor's orthostatic site, which enables downstream activation of both Gi1 and β-arrestin signaling (Fig. 6). As for the physiological function, FTY720, also known as fingolimod, a chemically modified version of myriocin, underscores the prominent of S1P signaling in regulating immune cell trafficking[91,92]. Due to its role in inhibiting lymphocyte egress, FTY720 was shown to reduce circulating lymphocytes by 70% (Fig.1). In contrast, SAR247799 demonstrated a comparable ability in activate downstream Gi1 signaling, but does not recruit β-arrestin like FTY720 (Fig. 6). Moreover, using $Tox1^{\Delta Cdh5}$ mice and $Arrb2^{\triangle Cdh5}$ mice, we confirmed that biased SAR247799 S1PR1-Gi activation is essential in endothelial barrier therapy for IBD treatment, (Fig. 7). Also, this SAR247799 binding pocket key amino acid S^{129} is conserved in amniotes (Supplementary Fig. 16a). SAR247799 can activate *Mus musculus* and *Homo sapiens* S1PR1 but not in *Carcharodon carcharias* fish S1PR1 (featuring A^{129}) Gi signaling (Supplementary Fig. 16b–d). In conjunction with our reciprocal mutation experiments, this suggested that S^{129} of S1PR1 is an important component for the SAR247799 binding pocket and activating Gi signaling (Supplementary Fig. 16b–d).

The spectrum of endothelial dysfunction-associated inflammatory diseases includes IBD, IPF, diabetes, psoriasis, hypertension, heart failure, renal failure, and atherosclerosis[50,68,93–96]. Endothelial dysfunction is set off by inflammation, an increase of reactive oxygen species (ROS) and reactive nitrogen species (RNS), cellular death, and decreased production of vasodilators, and is accompanied by enhanced generation of vasoconstrictors and vascular remodeling[2,3,68]. Targeting immune cells by immunosuppressive therapy is a common strategy for treating autoimmune or other inflammatory diseases[97,98], but the use of immunosuppressive drugs can increase infection susceptibility, decrease cancer immunosurveillance, and lower antibody production[97,99]. Our study confirmed that SAR247799 can also protect the endothelial barrier in other endothelial dysfunction-associated inflammatory diseases, such as IPF and COPD, without the aforementioned side effects (Fig. 8). Moreover, our study offers mechanistic insight into Gi-biased S1PR1 agonists and demonstrates that SAR247799, a Gi-biased S1PR1 agonist, is a feasible approach for endothelial dysfunction-associated disease treatment.

Methods
Patients and samples
The collection and utilization of paraffin-embedded colon sections from individuals with inflammatory bowel disease (IBD) and healthy controls were approved by the local Ethics Committee and Review Board of West China Hospital (Approval No. 2024[500]). The Ethics Review Committee waived the requirement for informed consent, as the study involved minimal risk to participants. Anonymization of samples was conducted by the Pathology Department of West China Hospital, and strict measures were taken to ensure privacy and confidentiality, none of our authors were involved in the collection of the paraffin-embedded tissues. The collection and use of colonic biopsies from IBD patients for the generation of organoids were approved by the local Ethics Committee and Review Board of West China Hospital (Approval No. 2023[1081]). Informed consent was written from all patients for the use of their tissue in this research. The basic information from the patients, including age, sex, and colitis location, is summarized in Supplementary Table 4.

Animals
Male C57BL/6 J wild-type mice, aged 6–8 weeks, were purchased from GemPharmatech Co., Ltd, Chengdu, China. $Tox1^{f/f}$ mice were constructed by Cyagen Biosciences Inc., China, and $Arrb2^{f/f}$ and $Rag2^{-/-}$ mice were constructed by GemPharmatech Co., Ltd, China with male mice aged 6–8 weeks used. The mice were housed in plastic cages with five animals per cage and fed with standard chow and water ad libitum in specific pathogen-free grade animal rooms. Mice were kept under a 12 h light/dark cycle-controlled atmosphere. The Animal Care and Use Committee of West China Hospital, Sichuan University approved all animal experimental procedures.

HUVEC culture and treatment
Human umbilical vein endothelial cells (HUVEC) obtained from the American Type Culture Collection (ATCC) were cultured in DMEM/F12 medium containing 10% fetal bovine serum and 1% penicillin/streptomycin at 37 °C under an atmosphere of 5% CO_2. The drug intervention group was treated with 1 µM SAR247799 for 18 h and then stimulated with 200 ng/ml TNF-α (novoprotein, Cat. No. C008). shRNA sequence: CAAGAGTATGTTTGTCGAAACAAACATACTCCCTTCCCGC. Cells were collected for mRNA detection after 24 h of treatment. Three biological replicates were performed.

Mouse colitis models, monitoring, and endoscopy
Colitis was induced with an oral administration of 2.5% (W/V) dextran sodium sulfate (DSS, MP Biomedicals, UK) in drinking water for the indicated period, after which the water containing DSS was replaced with normal drinking water. In TNBS experiments, colitis was induced in mice by intrarectal administration of 2.5% (w/v) TNBS (Sigma, p2297) in 50% ethanol. Mice were immunized with TNBS (150 µl) presensitization solution dissolved in acetone and olive oil in a 4:1 volume ratio by vortexing rigorously.

In the T cell adoptive transfer colitis model, naïve CD4$^+$ T cells were purified with fluorescence-activated cell sorting, labeled with fluorescent antibodies, and sorted for CD4$^+$, CD45RBhigh, and CD25$^-$ cells as the non-activated, naïve T cell population. Inject 2×10^5 naïve CD4$^+$ T cells intraperitoneally (i.p.) into the recipient $Rag2^{-/-}$ mice in a 200 µL volume of sterile PBS and monitoring disease progression for 4–6 weeks. Body weight and DAI scores were measured and recorded daily for each group of mice[100]. In all DSS experiments involving 5-ASA 100 mg/kg, FTY720 0.3 mg/kg, ozanimod 1 mg/kg (Selleck, China), and SAR247799 (Hebei Yaocheng Pharmaceutical Technology Co., Ltd) treatment, mice were assigned randomly to the vehicle or drug-treated groups. As determined from the multiple experiments conducted for colitis models, the effect sizes were very robust and good statistical outcomes were achievable. Colonoscopy was performed on experimental mice using a flexible video mini-endoscopic system (URF-V3; Olympus). Murine endoscopic index of colitis severity (MEICS) was used to score for colitis[101].

Bleomycin-induced pulmonary fibrosis-like mice model
To induce pulmonary fibrosis, C57BL/6 J mice (6–8 weeks old) were intratracheally injected with saline or bleomycin (Selleck, S1214) at a dose of 3 mg/kg body weight[102]. After the instillation, the anesthetized mice were kept 30 min on a warm bed for recovery. The experimental animals were monitored daily for adverse clinical signs, including body weight, appearance, hydration status, and behavioral changes. Following bleomycin injury, SAR247799 (1 mg/kg) and pirfenidone (300 mg/kg) were delivered by intragastric administration once per day for 14 days. On day 14, mice were sacrificed, lung tissues were collected for further measurements.

LPS and PPE induced COPD-like mice model
Mice were exposed to LPS and PPE to induce COPD-like injury[103]. Briefly, mice were lightly anesthetized with isoflurane prior to

intranasal delivery of PPE (1.2 U in 50 µl phosphate buffer saline [PBS] i.n.) and LPS (7 µg in 50 µl PBS i.n., both from Sigma-Aldrich) on day 1; this treatment regimen was performed for four consecutive weeks as shown in Fig. 8g. Control mice received the same volume of PBS on the indicated days. SAR247799 (1 mg/kg) administration was started 1 day before LPS/PPE injection and was administered by oral gavage daily for four weeks. Subsequently, the lungs were carefully excised after perfusion with ice-cold PBS and fixed in 4% paraformaldehyde for further use. Weight changes in mice were monitored daily during the experiments.

Quantitative real-time PCR (qRT-PCR)

Total RNA was extracted with TRIzol (Thermo Fisher Scientific) according to the manufacturer's protocol, followed by capillary electrophoresis quality control (NanoDrop 2000; Thermo Fisher Scientific). RNA (1 µg) was reverse transcribed using a PrimeScript RT reagent kit with gDNA Eraser (Takara Bio; RR047A). RT-PCR reactions were carried out with gene-specific primers (Qing Ke Bio, see Supplementary Table for primer sequences) mixed with SYBR Green PCR Master Mix (Takara Bio; RR820), according to the manufacturer's protocol. Samples were run in triplicates in a LightCycler 96 PCR system (Roche). mRNA expression was normalized using ACTB. Analysis was performed using the $\Delta\Delta Ct$ method. Primer was listed in Supplementary Table 5.

Histology, immunofluorescence staining

Human and mouse tissues were fixed with 4% paraformaldehyde in PBS, embedded in paraffin, sectioned, and stained. The collection and utilization of paraffin-embedded colon sections from individuals with IBD and healthy controls were approved by the local Ethics Committee and Review Board of West China Hospital (Approval No. 2024[500]). Histopathological analysis of paraffin-embedded was performed in lung sections stained with Masson's trichrome staining and periodic acid-Schiff (PAS) staining using standard procedures. Immunofluorescence was performed on formalin-fixed, paraffin-embedded colon tissues. For immunofluorescence, samples were cryosectioned, blocked, and then stained with S1PR1 (MA5-32587, Invitrogen), CD31 (ab281583, Abcam), CD3 (17617-1-AP, proteintech), Vcam1 (MA5-11447, Invitrogen), Icam1 (ab171123, Abcam) and E-selectin (PA5-106911, Invitrogen) antibody. Images were captured using an Olympus BX600 microscope (Olympus Corporation, Tokyo, Japan) and SPOT Flex camera (Olympus Corporation, Tokyo, Japan) and were analyzed with ImagePro Plus (version 6.0, Media Cybernetics) software. The scores of inflammatory infiltrations, lesion depth, crypt destruction, and lesion range were evaluated[47].

Evans blue assay for endothelial permeability

Evans blue dye (Sigma-Aldrich, 20 mg/kg in 100 µl PBS) was injected via the tail vein of the mice. After 30 min of injection, mice were anesthetized with isoflurane, and the distal two-thirds of the colons were examined using a small-animal video endoscope (URF-V3, Olympus). The colon tissues were then harvested, weighted and incubated in 1 mL of formamide (Sigma-Aldrich) at 55 °C overnight. The Evans blue dye was extracted from colon tissues with formamide and was measured by absorbance at 620 nm according to a standard curve. Vascular endothelial permeability was calculated as the weight of Evans blue dye in one gram of colon tissues.

Hydroxyproline assay

Hydroxyproline levels in the upper lobe of the right lungs were determined by alkaline hydrolysis using a kit from Nanjing Jiancheng Bioengineering Institute (Nanjing, China) according to the manufacturer's instructions.

Flow cytometry

After the animal experiment, lamina propria mononuclear cells (LPMC) were isolated from mice with fresh colonic lamina propria suffering from different treatments as previously described[104]. In brief, the colons were exercised, cut along the intestinal axis, washed with cold PBS twice, and cut into small pieces. Then the small colon specimens were incubated in Ca/Mg-free Hank's balanced salt solution (HBSS, Sigma-Aldrich) containing 30 mM ethylenediminetetraacetic acid (EDTA, Sigma-Aldrich) and 1.5 mM dithiothreitol (DDT, Sigma-Aldrich) three times at 37 °C for 10 min under shaking. After that, LPMCs were isolated from the remaining tissue. The tissues were digested in a shaker with RPMI (Gibco) medium contain 20% FBS, 1 mg/mL collagenase IV, and 0.05 mg/mL DNAase at 37 °C for 30 min. Subsequently, the samples were filtered through 40 µm cell strainers, washed using PBS, resuspended in 4 mL 40% Percoll (Sigma-Aldrich), and slowly added over an 80% Percoll solution. The mononuclear cell suspensions from 40–80% Percoll interface were harvested, and LPMCs were obtained by centrifugation at 500 × g and 4 °C for 8 min. Finally, the cells were blocked and stained with fluorescently label monoclonal antibodies for 30 min at 4 °C in the dark, and the antibodies as follows: anti-CD45-BV510, anti-CD3-AF700, anti-CD4-BV650, anti-CD8-BV785, anti-FVS-APC-cy7 (all antibodies from eBioscience). The final cells were measured on a Cytek Aurora (BD, Biosciences) and analyzed with FlowJo10 software. To evaluate immunophenotypic analyses of PBMCs from mouse peripheral blood, the cells were stained using the antibodies described above.

Colonic biopsies organoid culture

De-identified endoscopic tissue biopsies were collected from grossly unaffected (macroscopically regular) areas of the colon in patients undergoing endoscopy for gastrointestinal complaints. The collection and use of colonic biopsies from IBD patients for the generation of organoids were approved by the local Ethics Committee and Review Board of West China Hospital (Approval No. 2023[1081]). Informed consent was written from all patients for the use of their tissue in this research. Tissue was digested in 2 mg/ml collagenase I for 40 min at 37 °C followed by mechanical dissociation, and isolated crypts were resuspended in growth factor-reduced Matrigel (Becton Dickinson) and polymerized at 37 °C. Organoids were grown in expansion medium consisting of advanced DMEM F12 supplemented with L-WRN conditioned medium (50% vol/vol, ATCC, *cat*. no. CRL-3276), glutamax (Thermo, 35050061), 20 mM HEPES (Gibco, 15630130), murine epidermal growth factor (50 ng/ml), N2 supplement, B27 supplement, 10 nM human [Leu15]-gastrin I, 1 mM n-acetyl cysteine, 10 mM nicotinamide, 10 µM SB202190, 500 nM A83-01[105].

mRNA sequencing

RNA from tissues was extracted using the peqGOLD total RNA kit (VWR International). RNA integrity and quantity were assessed using the Nanodrop. Qubit RNA HS assay and the Bioanalyzer 2100 system (Agilent Technologies). A total amount of 1 µg RNA per sample was used as input material for the RNA sample preparations. Sequencing libraries were generated using NEBNext Ultra RNA Library Prep Kit for Illumina (New England Biolabs) following the manufacturer's recommendations and index codes were added to attribute sequences to each sample. PCR was performed with Phusion High-Fidelity DNA polymerase (New England Biolabs), Universal PCR primers, and Index Primer. PCR products were purified (AMPure XP system), and library quality was assessed on the Agilent Bioanalyzer 2100 system. The clustering of the index-coded samples was performed on a cBot Cluster Generation System using PE Cluster Kit cBot-HS (Illumina) according to the manufacturer's instructions. After cluster generation, the library preparations were sequenced on an Illumina platform, and paired-end reads were generated.

Clean data (clean reads) were obtained by removing reads containing adapter and poly-N sequences and reads with low quality from raw data. At the same time, Q20, Q30, and GC content of the clean data were calculated. All downstream analyses were based on clean data with high quality. Reference genome and gene model annotation files were downloaded from the genome browser website (National Center for Biotechnology Information, University of California Santa Cruz or Ensemble). Paired-end clean reads were mapped to the reference genome using HISAT2 software (version 2.0.5). featureCounts (version 1.5.0-p3) was used to count the read numbers mapped for each gene. Transcript per Kilobase per Million mapped reads (TPM) of each gene were calculated on the basis of the length of the gene and reads counts mapped to this gene. TPM considers the effect of sequencing depth and gene length for the read counts at the same time and is currently the most commonly used method.

RNA-seq and scRNA-seq analysis

Differential gene expression analysis for expression profiling by array with Student's t test and for raw counts with DESeq2 (version 1.38.3) in R (version 4.2.3). concurrently, non-duplicate samples were analyzed using GFOLD (version 1.1.4) for differential gene expression analysis. The cutoff criteria for identifying differentially expressed genes (DEGs) were set as follows: $P < 0.05$ and $|logFC| \geq 1$ or $|GFOLD| \geq 2$ and E-FDR $= 1$ (for non-duplicate samples). GOBP and KEGG enrichment analyses were carried out by clusterProfiler (version 4.6.2) package of R. Download the GOBP datasets from MSigDB (Molecular Signatures Database), and used RNA-seq data for GSVA analysis using the R package GSVA (version 1.46.0). We utilized the mMCP-counter (version 1.1.0) package in R to estimate the composition of immune and stromal cells in murine samples, aiming to assess the infiltration of stromal and immune cells in the RNA-seq data. scRNA-seq data were processed and analyzed with the R package Seurat (version 4.0.5).

Constructs

The truncated human *S1PR1* genes (UniProt code: P21453) with residues 1–338 were cloned into the pFastBac1 vector for protein expression. To facilitate S1PR1 receptor expression and purification, A haemagglutinin (HA) signal sequence, a Flag epitope tag sequence, and T4 lysozyme (T4L) were sequentially fused at the N-terminus of the receptor[106]. The human full-length $G\alpha_{i1}$ with four dominant-negative mutations (S47N, G203A, E245A, A326S) were cloned into the pFastBac1 vector[107,108]. Human full-length $G\beta_1$ with the N-terminal hexahistidine-tag and the human full-length $G\gamma_2$ were cloned into the pFastBac-Dual vector (Invitrogen). For the BRET-based Gi1 dissociation assay, the full-length human S1PR1 genes were cloned into the pcDNA3.1 vector, with the hemagglutinin (HA) signal peptide and Flag tag in the N terminus of the receptor. NanoLuc (Nluc) was fused to $G\alpha_{i1}$-Nluc, and mVenus was fused at the N terminus of $G\gamma_2$. For the NanoBiT β-arrestin2 recruitment assay, Nluc was split into a large fragment (LgBiT) and a small fragment (SmBiT). The LgBiT and SmBiT was fused to the C-terminus of S1PR1 and to the N terminus of β-arrestin2, respectively. The mutants of S1PR1 for functional assays were generated using the ClonExpress II One Step Cloning Kit (Vazyme Biotech, C214-01).

Expression and purification of S1PR1-Gi complexes

The Bac-to-Bac Baculovirus Expression System was used to generate high-quality recombinant baculoviruses and express the S1PR1-Gi complexes in this study. The *Spodoptera frugiperda* Sf9 insect cells were coinfected the S1PR1, $G\alpha_{i1}$ and $G\beta_1/G\gamma_2$ baculoviruses at a 1:1:1 ratio when cell density was 2.7×10^6 cells per mL and cultured at 27 °C, 140 rpm for 48 h. Then, the infected cells were collected by centrifugation at $2000 \times g$ for 10 min, and the

pellets were stored at -80 °C for further purification. To prepare the S1PR1-Gi complexes, the pellets were resuspended with lysis buffer containing 20 mM HEPES pH 7.5, 50 mM NaCl, 5 mM $CaCl_2$, 5 mM $MgCl_2$, 25 mU/ mL apyrase (NEB), protease inhibitors (100 µg/mL leupeptin, 160 µg/mL benzamidine) and 40 µM SAR247799 and incubated for 2 h at room temperature. The cell pellets were collected at $22,000 \times g$ centrifugation for 10 min and solubilized in buffer containing 20 mM HEPES pH 7.5, 100 mM NaCl, 25 mU/mL apyrase, protease inhibitors,10% (w/v) glycerol, 1% (w/v) lauryl maltose neopentyl glycol (LMNG), 0.2% (w/v) cholesteryl hemisuccinate (CHS) and 40 µM SAR247799 for 2 h at 4 °C. After centrifugation at $65,000 \times g$ for 20 min, the supernatant was collected and incubated with M1 anti-FLAG antibody resin (Sigma-Aldrich) for 2 h at 4 °C. The resin was washed with 20 column volumes of wash buffer containing 20 mM HEPES pH 7.5, 100 mM NaCl, 0.00375% (w/v) LMNG, 0.00075% (w/v) CHS, 5% glycerol, 40 µM SAR247799 and protease inhibitors. The complex was eluted with the wash buffer supplemented with 10 mM EDTA and 0.2 mg/mL Flag peptide followed by concentration and subjected into a Superpose 6 Increase 10/300 GL (Cytiva) size-exclusion chromatography (SEC) column with SEC buffer containing 20 mM HEPES pH 7.5, 100 mM NaCl, 0.00375% (w/v) LMNG, 0.00125% (w/v) GDN, 0.00075% (w/v) CHS, 5% glycerol, 40 µM SAR247799, and protease inhibitors. The peak fractions of S1PR1-Gi complexes from SEC were collected and concentrated using an Amicon Ultra Centrifugal Filter (MWCO, 100 kDa).

Cryo-EM specimen preparation

For cryo-EM grids preparation, three microliters of the purified SAR247799-S1PR1-Gi complex were applied onto glow-discharged holey carbon grids (300 mesh R1.2/1.3, Quantifoil). After a 2.5 s bolting with the paraments of 100% humidity at 4 °C, the grids were plunge-frozen into liquid ethane using Vitrobot Mark IV (Thermo Fisher).

The prepared grid was transferred to Titan Krios cryo-electron microscope (Thermo Fisher) equipped Gatan K2 Summit detector. The micrographs were collected at 300 kV with a nominal magnification of $\times 165,000$ and a pixel size of 0.85 Å. The total exposure dose was 65.1 $e^-/Å^{-2}$, with a defocus ranging from -1.0 µm–1.8 µm, and 40 frames were recorded for each movie stack.

Data processing and map construction

For the SAR247799-S1PR1-Gi complex, 4652 movie stacks were motion-corrected using MotionCor2[109] and estimated the Contrast Transfer Function(CTF) parameters by Gctf[110]. Particles were auto-picked using RELION-4.0[111], yielding 1,974,519 particles. After a round of 2D classification, 1,479,292 particles were retained. The retained particles underwent rounds of Ab-Initio reconstruction and heterogeneous refinement in cryo-SPARC[112]. The best class characterized by high-quality complex density containing 215,808 particles, was selected for non-uniform refinement and local refinement, resulting in a map with a global resolution of 3.47 Å at a Fourier shell correlation of 0.143. The process procedure is shown in Supplementary Fig. 11.

Model building and structure refinement

The initial model for the S1PR1-Gi complex was generated using the cryo-EM structure of the siponimod-bound S1PR1-Gi complex (PDB ID: 7EVY). After model fitted into the corresponding EM density maps using UCSF chimera X[113], the real-space refinement and manual adjustment were performed by Coot[114] and Phenix[115]. The structural diagrams in Figs were performed by PyMol and UCSF Chimera X.

Molecular dynamics (MD) simulation

The initial model of receptor-ligand complex for MD simulation was taken from this paper. Two pseudo positions of ligand were also used

for simulation. All models were oriented by running PPM 2.0 (PMID: 21890895) and embedded into 75% palmitoyl-oleoyl-phosphatidylcholine (POPC)-25% cholesterol lipid bilayers in cuboid shapes with dimensions of approximately 7.5 nm × 7.5 nm × 10.0 nm. The simulation systems were supplemented with an ion concentration of 0.15 M NaCl, solvated in the TIP3P water model, and neutralized by replacing water molecules with ions. All the MD simulation systems were constructed using the CHARMM-GUI[116,117] web interface utilizing the CHARMM36m[118] force field and performed GROMACS 2022.3 package[119]. Every atom was assigned a velocity randomly and independently in the systems. The steepest descent algorithm was employed to minimize the energy of the system. To equilibrate the system, an NVT ensemble was run for 2500 ps with a time step of 1 fs, followed by an NPT ensemble at 310.15 K and 1 bar. The final systems were undergoing an MD simulation for 200,000 ps at 310.15 K and 1 bar. The $gmx\ rms$ utility was used to analyze the RMSD and distance of the trajectory.

BRET-based $G\alpha_{i1}$-$G\gamma_2$ dissociation assay

S1PR1-mediated $G\alpha_{i1}$ protein signaling was monitored by BRET-based $G\alpha_{i1}$-$G\gamma_2$ dissociation assay[120]. In brief, CHO cells (American Type Culture Collection, ATCC) were transfected with a mixture of the receptor, pcDNA3.1-$G\alpha_{i1}$-Nluc, pcDNA3.1-$G\beta_1$ and pcDNA3.1-$G\gamma_2$-mVenus using PEI transfection reagent (YEASEN, 40816ES02). After one day of transfection, cells were seeded into white flat-bottom 96-well plates. The next day, the medium was removed and replaced with HBSS buffer (containing 20 mM HEPES, 5 μM coelenterazine h). The BRET signals were measured by the Synergy H1 microplate reader (BioTek) after incubation for 30 min at room temperature. The BRET signal was calculated as the ratio of light emission at 540 nm/460 nm. Data analysis was performed using a simulation dose-response in GraphPad Prism 9.0.

NanoBiT β-arrestin recruitment assay

S1PR1-mediated β-arrestin recruitment was measured by the NanoBiT β-arrestin recruitment assay[107]. The C-terminal of S1PR1 was linked with LgBiT, and the β-arrestin2 was inserted into SmBiT at the N-terminus. These vectors were transfected into CHO cells at a ratio of 1:1. After one day of growth, the transfected cells were seeded into 96-well white plates. The next day, the growth medium was substituted with HBSS buffer (containing 20 mM HEPES, pH 7.4, with 5 μM coelenterazine h). After a 30 min incubation, the luminescence signals were measured by the Synergy H1 microplate reader (BioTek). Data were processed using GraphPad Prism 9.0.

NanoBiT-based internalization assay

Agonist-induced S1PR1 internalization was examined by a NanoBiT-based internalization assay[108]. The assay required modification of the N-terminus of the FYVE domain with LgBiT and modification of the N-terminus of β-arrestin2 with SmBiT. After 24 h transient transfection with S1PR1 wild-type, pcDNA3.1-LgBiT-FYVE, and pcDNA3.1-SmBiT-β-arrestin2, cells were replated into 96-well plates. The following day, the culture medium was removed and HBSS buffer (containing 20 mM HEPES, pH 7.4, with 5 μM coelenterazine h) was added. After incubating for 1 h at room temperature, the luciferase intensity was read on the Synergy H1 microplate reader (BioTek) using the luciferase program. Data were processed using the nonlinear regression dose-response curves in GraphPad Prism 9.0.

Enzyme-linked immunosorbent assay (ELISA)

To measure the cell surface expression of S1PR1 and mutants, ELISA assay was performed. Briefly, S1PR1 wild-type and mutants with a FLAG tag attached to the N-terminus were expressed in CHO cells. Cells were seeded in Poly-L-Lysine coated 96-well plates and grown overnight at 37 °C, 5% CO_2. The next day, cells were washed with PBS twice and fixed with 4% (w/v) formaldehyde for 10 min. Then, cells were blocked with 5% (w/v) BSA at room temperature for 1 h. Next, anti-FLAG M2-HRP conjugate was added to the plates (1:2,000, Sigma-Aldrich). After 1 h incubation, cells were washed with PBS and incubated with HRP substrate 3,3′,5,5′-tetramethyl benzidine (TMB). The reaction was terminated by 2 M H_2SO_4. The luminescence was measured using the Synergy H1 microplate reader (BioTek). Values were normalized to the wild-type receptor and graphed as a percentage of wild-type using GraphPad Prism 9.0.

Statistical analysis

Box plots in this study represent display the median (horizontal line), the 25th percentile (lower bound of the box), and the 75th percentile (upper bound of the box). Whiskers represent 1.5 times the interquartile range (IQR), and individual data points are shown as jittered dots. Statistical significance between groups is indicated by horizontal lines and p-values. Data points are color-coded based on group identity. Except for the RNA-seq data and scRNA-seq data analyzed using R for downstream analysis, all data were presented as means ± standard error of the mean (SEM) and analyzed using GraphPad Prism 9.0 program (GraphPad Software, San Diego, Canada). Data between two groups were compared using a two-sided Student's t test, and data from more than two groups were compared using two-way ANOVA with multiple comparisons. Spearman's rank correlation analysis was used for correlation analysis. The adjusted P below 0.05 was considered statistically significant.

Reporting summary

Further information on research design is available in the Nature Portfolio Reporting Summary linked to this article.

Data availability

The single-particle cryo-EM coordinates and density map of SAR247799-S1PR1-Gi have been deposited at the PDB and the Electron Microscopy Data Bank under accession codes 8YIC and EMD-39313, respectively. Microarray and scRNA-seq data were obtained from the Gene Expression Omnibus (GEO), with the following accession codes: GSE66407 (https://www.ncbi.nlm.nih.gov/geo/query/acc.cgi?acc=GSE66407), GSE59071, GSE114374, GSE148794, GSE231993, GSE132771 (https://www.ncbi.nlm.nih.gov/geo/query/acc.cgi?acc=GSE132771), GSE213017, GSE17154.

The RNA-seq data from E-MTAB-9850 were obtained from ArrayExpress. The RNA-seq data for mouse colons and human intestinal organoids generated in this study have been deposited in the Genome Sequence Archive (GSA) database under the accession codes "CRA017842" (https://ngdc.cncb.ac.cn/gsa/search?searchTerm=CRA017842) and "HRA008746" (https://ngdc.cncb.ac.cn/search/specific?db=hra&q = HRA008746), respectively. The data supporting the findings from this study are available within the manuscript and its supplementary information. Source data are provided in this paper.

Code availability

All code used to generate and analyze the data in this study utilizes standard commands with publicly available platforms; no custom code was utilized.

References

1. Wardlaw, J. M., Smith, C. & Dichgans, M. Small vessel disease: mechanisms and clinical implications. *Lancet Neurol.* **18**, 684–696 (2019).
2. Bazzoni, G. & Dejana, E. Endothelial cell-to-cell junctions: molecular organization and role in vascular homeostasis. *Physiol. Rev.* **84**, 869–901 (2004).

3. Cong, X. & Kong, W. Endothelial tight junctions and their regulatory signaling pathways in vascular homeostasis and disease. *Cell Signal* **66**, 109485 (2020).

4. Wettschureck, N., Strilic, B. & Offermanns, S. Passing the Vascular Barrier: Endothelial Signaling Processes Controlling Extravasation. *Physiol. Rev.* **99**, 1467–1525 (2019).

5. Rafii, S., Butler, J. M. & Ding, B. S. Angiocrine functions of organ-specific endothelial cells. *Nature* **529**, 316–325 (2016).

6. Jourde-Chiche, N. et al. Endothelium structure and function in kidney health and disease. *Nat. Rev. Nephrol.* **15**, 87–108 (2019).

7. Danese, S. Role of the vascular and lymphatic endothelium in the pathogenesis of inflammatory bowel disease: 'brothers in arms. *Gut* **60**, 998–1008 (2011).

8. Moss, B. J., Ryter, S. W. & Rosas, I. O. Pathogenic Mechanisms Underlying Idiopathic Pulmonary Fibrosis. *Annu. Rev. Pathol.* **17**, 515–546 (2022).

9. Spalinger, J. et al. Doppler US in patients with crohn disease: vessel density in the diseased bowel reflects disease activity. *Radiology* **217**, 787–791 (2000).

10. Scaldaferri, F. et al. The role of MAPK in governing lymphocyte adhesion to and migration across the microvasculature in inflammatory bowel disease. *Eur. J. Immunol.* **39**, 290–300 (2009).

11. Danese, S. et al. TNF-alpha blockade down-regulates the CD40/CD40L pathway in the mucosal microcirculation: a novel anti-inflammatory mechanism of infliximab in Crohn's disease. *J. Immunol.* **176**, 2617–2624 (2006).

12. Yacyshyn, B. R. Adhesion molecule therapeutics in IBD. *Inflamm. Bowel Dis.* **14**, S279–S280 (2008).

13. Bouma, G. & Strober, W. The immunological and genetic basis of inflammatory bowel disease. *Nat. Rev. Immunol.* **3**, 521–533 (2003).

14. Martinez, F. J. et al. Idiopathic pulmonary fibrosis. *Nat. Rev. Dis. Prim.* **3**, 17074 (2017).

15. Kotas, M. E. & Medzhitov, R. Homeostasis, inflammation, and disease susceptibility. *Cell* **160**, 816–827 (2015).

16. Hodson, R. Inflammatory bowel disease. *Nature* **540**, S97 (2016).

17. Richeldi, L., Collard, H. R. & Jones, M. G. Idiopathic pulmonary fibrosis. *Lancet* **389**, 1941–1952 (2017).

18. Al-Bawardy, B., Shivashankar, R. & Proctor, D. D. Novel and emerging therapies for inflammatory bowel disease. *Front. Pharm.* **12**, 651415 (2021).

19. Danese, S. & Fiocchi, C. Endothelial cell-immune cell interaction in IBD. *Dig. Dis.* **34**, 43–50 (2016).

20. Salmi, M. & Jalkanen, S. Endothelial ligands and homing of mucosal leukocytes in extraintestinal manifestations of IBD. *Inflamm. Bowel Dis.* **4**, 149–156 (1998).

21. Huang, B. et al. Mucosal profiling of pediatric-onset colitis and IBD reveals common pathogenics and therapeutic pathways. *Cell* **179**, 1160–1176 (2019).

22. Rosen, H. & Goetzl, E. J. Sphingosine 1-phosphate and its receptors: an autocrine and paracrine network. *Nat. Rev. Immunol.* **5**, 560–570 (2005).

23. Rivera, J., Proia, R. L. & Olivera, A. The alliance of sphingosine-1-phosphate and its receptors in immunity. *Nat. Rev. Immunol.* **8**, 753–763 (2008).

24. Rosen, H., Gonzalez-Cabrera, P. J., Sanna, M. G. & Brown, S. Sphingosine 1-phosphate receptor signaling. *Annu. Rev. Biochem.* **78**, 743–768 (2009).

25. Marsolais, D. & Rosen, H. Chemical modulators of sphingosine-1-phosphate receptors as barrier-oriented therapeutic molecules. *Nat. Rev. Drug Discov.* **8**, 297–307 (2009).

26. Wang, X., Chen, S., Xiang, H., Liang, Z. & Lu, H. Role of sphingosine-1-phosphate receptors in vascular injury of inflammatory bowel disease. *J. Cell Mol. Med.* **25**, 2740–2749 (2021).

27. Wang, J. et al. Review article: the sphingosine 1 phosphate/sphingosine 1 phosphate receptor axis - a unique therapeutic target in inflammatory bowel disease. *Aliment Pharm. Ther.* **55**, 277–291 (2022).

28. Shiow, L. R. et al. CD69 acts downstream of interferon-alpha/beta to inhibit S1P1 and lymphocyte egress from lymphoid organs. *Nature* **440**, 540–544 (2006).

29. Schwab, S. R. & Cyster, J. G. Finding a way out: lymphocyte egress from lymphoid organs. *Nat. Immunol.* **8**, 1295–1301 (2007).

30. Visentin, B. et al. Validation of an anti-sphingosine-1-phosphate antibody as a potential therapeutic in reducing growth, invasion, and angiogenesis in multiple tumor lineages. *Cancer Cell* **9**, 225–238 (2006).

31. Nagahashi, M. et al. Targeting the SphK1/S1P/S1PR1 axis that links obesity, chronic inflammation, and breast cancer metastasis. *Cancer Res.* **78**, 1713–1725 (2018).

32. Sandborn, W. J. et al. Ozanimod as induction and maintenance therapy for Ulcerative Colitis. *N. Engl. J. Med.* **385**, 1280–1291 (2021).

33. Sandborn, W. J. et al. Ozanimod induction and maintenance treatment for Ulcerative Colitis. *N. Engl. J. Med.* **374**, 1754–1762 (2016).

34. Cohen, J. A. & Chun, J. Mechanisms of fingolimod's efficacy and adverse effects in multiple sclerosis. *Ann. Neurol.* **69**, 759–777 (2011).

35. Paik, J. Ozanimod: A review in Ulcerative Colitis. *Drugs* **82**, 1303–1313 (2022).

36. Gaengel, K. et al. The sphingosine-1-phosphate receptor S1PR1 restricts sprouting angiogenesis by regulating the interplay between VE-cadherin and VEGFR2. *Dev. Cell* **23**, 587–599 (2012).

37. Nitzsche, A. et al. Endothelial S1P(1) signaling counteracts infarct expansion in ischemic stroke. *Circ. Res.* **128**, 363–382 (2021).

38. Hao, M. et al. S1PR1 serves as a viable drug target against pulmonary fibrosis by increasing the integrity of the endothelial barrier of the lung. *Acta Pharm. Sin. B* **13**, 1110–1127 (2023).

39. Poirier, B. et al. A G protein-biased S1P(1) agonist, SAR247799, protects endothelial cells without affecting lymphocyte numbers. *Sci. Signal* **13**, https://doi.org/10.1126/scisignal.aax8050 (2020).

40. Bergougnan, L. et al. First-in-human study of the safety, tolerability, pharmacokinetics and pharmacodynamics of single and multiple oral doses of SAR247799, a selective G-protein-biased sphingosine-1 phosphate receptor-1 agonist for endothelial protection. *Br. J. Clin. Pharm.* **87**, 598–611 (2021).

41. Wirtz, S. et al. Chemically induced mouse models of acute and chronic intestinal inflammation. *Nat. Protoc.* **12**, 1295–1309 (2017).

42. Cartier, A. & Hla, T. Sphingosine 1-phosphate: Lipid signaling in pathology and therapy. *Science* **366**, https://doi.org/10.1126/science.aar5551 (2019).

43. Zhou, Q. et al. Common activation mechanism of class A GPCRs. *Elife* **8**, https://doi.org/10.7554/eLife.50279 (2019).

44. Hanson, M. A. et al. Crystal structure of a lipid G protein-coupled receptor. *Science* **335**, 851–855 (2012).

45. Akasaka, H. et al. Structure of the active G(i)-coupled human lysophosphatidic acid receptor 1 complexed with a potent agonist. *Nat. Commun.* **13**, 5417 (2022).

46. Liu, S. et al. Differential activation mechanisms of lipid GPCRs by lysophosphatidic acid and sphingosine 1-phosphate. *Nat. Commun.* **13**, 731 (2022).

47. Yu, L. et al. Structural insights into sphingosine-1-phosphate receptor activation. *Proc. Natl. Acad. Sci. USA* **119**, e2117716119 (2022).

48. Xu, Z. et al. Structural basis of sphingosine-1-phosphate receptor 1 activation and biased agonism. *Nat. Chem. Biol.* **18**, 281–288 (2022).

49. Heydenreich, F. M. et al. Molecular determinants of ligand efficacy and potency in GPCR signaling. *Science* **382**, eadh1859 (2023).

50. May, J., Mitchell, J. A. & Jenkins, R. G. Beyond epithelial damage: vascular and endothelial contributions to idiopathic pulmonary fibrosis. *J. Clin. Invest.* **133**, https://doi.org/10.1172/JCI172058 (2023).

51. Peinado, V. I. et al. Endothelial dysfunction in pulmonary arteries of patients with mild COPD. *Am. J. Physiol.* **274**, L908–L913 (1998).

52. Rangarajan, S. et al. Metformin reverses established lung fibrosis in a bleomycin model. *Nat. Med.* **24**, 1121–1127 (2018).

53. Bindu, S., Mazumder, S. & Bandyopadhyay, U. Non-steroidal anti-inflammatory drugs (NSAIDs) and organ damage: A current per-spective. *Biochem. Pharm.* **180**, 114147 (2020).

54. Cunningham, C. & Skelly, D. T. Non-steroidal anti-inflammatory drugs and cognitive function: are prostaglandins at the heart of cognitive impairment in dementia and delirium? *J. Neuroimmune Pharm.* **7**, 60–73 (2012).

55. Fenis, A., Demaria, O., Gauthier, L., Vivier, E. & Narni-Mancinelli, E. New immune cell engagers for cancer immunotherapy. *Nat. Rev. Immunol.* https://doi.org/10.1038/s41577-023-00982-7 (2024).

56. Bender, E. Cancer immunotherapy. *Nature* **552**, S61 (2017).

57. Hernandez, R., Poder, J., LaPorte, K. M. & Malek, T. R. Engineering IL-2 for immunotherapy of autoimmunity and cancer. *Nat. Rev. Immunol.* **22**, 614–628 (2022).

58. Pauken, K. E., Dougan, M., Rose, N. R., Lichtman, A. H. & Sharpe, A. H. Adverse events following cancer immunotherapy: Obstacles and opportunities. *Trends Immunol.* **40**, 511–523 (2019).

59. Kennedy, L. B. & Salama, A. K. S. A review of cancer immu-notherapy toxicity. *CA Cancer J. Clin.* **70**, 86–104 (2020).

60. Chhabra, N. & Kennedy, J. A review of cancer immunotherapy toxicity: Immune checkpoint inhibitors. *J. Med. Toxicol.* **17**, 411–424 (2021).

61. Baluna, R. & Vitetta, E. S. Vascular leak syndrome: a side effect of immunotherapy. *Immunopharmacology* **37**, 117–132 (1997).

62. Naschberger, E. et al. Analysis of the interferon-gamma-induced secretome of intestinal endothelial cells: putative impact on epi-thelial barrier dysfunction in IBD. *Front. Cell Dev. Biol.* **11**, 1213383 (2023).

63. Cibor, D. et al. Endothelial dysfunction in inflammatory bowel diseases: Pathogenesis, assessment and implications. *World J. Gastroenterol.* **22**, 1067–1077 (2016).

64. Bamias, G., Pizarro, T. T. & Cominelli, F. Immunological regulation of intestinal fibrosis in inflammatory bowel disease. *Inflamm. Bowel Dis.* **28**, 337–349 (2022).

65. Lee, C. H., Koh, S. J., Radi, Z. A. & Habtezion, A. Animal models of inflammatory bowel disease: novel experiments for revealing pathogenesis of colitis, fibrosis, and colitis-associated colon cancer. *Intest. Res.* **21**, 295–305 (2023).

66. Li, J. et al. Mouse models of intestinal fibrosis. *Methods Mol. Biol.* **2299**, 385–403 (2021).

67. Zhang, M. et al. Anti-vascular endothelial growth factor therapy in breast cancer: Molecular pathway, potential targets, and current treatment strategies. *Cancer Lett.* **520**, 422–433 (2021).

68. Xu, S. et al. Endothelial dysfunction in atherosclerotic cardiovas-cular diseases and beyond: From mechanism to pharma-cotherapies. *Pharm. Rev.* **73**, 924–967 (2021).

69. Price, M. O., Mehta, J. S., Jurkunas, U. V. & Price, F. W. Jr Corneal endothelial dysfunction: Evolving understanding and treatment options. *Prog. Retin. Eye Res.* **82**, 100904 (2021).

70. Barbier, V. et al. Endothelial E-selectin inhibition improves acute myeloid leukaemia therapy by disrupting vascular niche-mediated chemoresistance. *Nat. Commun.* **11**, 2042 (2020).

71. Wong, M. T. et al. A high-dimensional atlas of human T cell diversity reveals tissue-specific trafficking and cytokine sig-natures. *Immunity* **45**, 442–456 (2016).

72. Tyring, S. K. et al. Risankizumab in patients with moderate-to-severe atopic dermatitis: A phase 2, randomized, double-blind, placebo-controlled study. *Dermatol Ther.* **13**, 595–608 (2023).

73. Strachan, R. T. et al. Divergent transducer-specific molecular efficacies generate biased agonism at a G protein-coupled receptor (GPCR). *J. Biol. Chem.* **289**, 14211–14224 (2014).

74. Li, T. et al. Homocysteine directly interacts and activates the angiotensin II type I receptor to aggravate vascular injury. *Nat. Commun.* **9**, 11 (2018).

75. Liu, C. H. et al. Arrestin-biased AT1R agonism induces acute catecholamine secretion through TRPC3 coupling. *Nat. Commun.* **8**, 14335 (2017).

76. Yang, F. et al. Structural basis of GPBAR activation and bile acid recognition. *Nature* **587**, 499–504 (2020).

77. Kim, J. et al. The beta-arrestin-biased beta-adrenergic receptor blocker carvedilol enhances skeletal muscle contractility. *Proc. Natl. Acad. Sci. USA* **117**, 12435–12443 (2020).

78. Ma, L. et al. Structural basis and molecular mechanism of biased GPBAR signaling in regulating NSCLC cell growth via YAP activity. *Proc. Natl. Acad. Sci. USA* **119**, e2117054119 (2022).

79. Suomivuori, C. M. et al. Molecular mechanism of biased signaling in a prototypical G protein-coupled receptor. *Science* **367**, 881–887 (2020).

80. Wingler, L. M. et al. Angiotensin and biased analogs induce structurally distinct active conformations within a GPCR. *Science* **367**, 888–892 (2020).

81. Wootten, D., Christopoulos, A., Marti-Solano, M., Babu, M. M. & Sexton, P. M. Mechanisms of signalling and biased agonism in G protein-coupled receptors. *Nat. Rev. Mol. Cell Biol.* **19**, 638–653 (2018).

82. Pham, T. H., Okada, T., Matloubian, M., Lo, C. G. & Cyster, J. G. S1P1 receptor signaling overrides retention mediated by G alpha i-coupled receptors to promote T cell egress. *Immunity* **28**, 122–133 (2008).

83. Grigorova, I. L. et al. Cortical sinus probing, S1P1-dependent entry and flow-based capture of egressing T cells. *Nat. Immunol.* **10**, 58–65 (2009).

84. Burg, N., Salmon, J. E. & Hla, T. Sphingosine 1-phosphate receptor-targeted therapeutics in rheumatic diseases. *Nat. Rev. Rheumatol.* **18**, 335–351 (2022).

85. Xiong, Y. et al. CD4 T cell sphingosine 1-phosphate receptor (S1PR) 1 and S1PR4 and endothelial S1PR2 regulate afferent lymphatic migration. *Sci. Immunol.* **4**, https://doi.org/10.1126/sciimmunol.aav1263 (2019).

86. Cyster, J. G. & Schwab, S. R. Sphingosine-1-phosphate and lym-phocyte egress from lymphoid organs. *Annu.Rev. Immunol.* **30**, 69–94 (2012).

87. Simmons, S. & Ishii, M. Sphingosine-1-phosphate: a master reg-ulator of lymphocyte egress and immunity. *Arch. Immunol. Ther. Exp.* **62**, 103–115 (2014).

88. Matloubian, M. et al. Lymphocyte egress from thymus and per-ipheral lymphoid organs is dependent on S1P receptor 1. *Nature* **427**, 355–360 (2004).

89. Cantalupo, A. et al. S1PR1 (Sphingosine-1-Phosphate Receptor 1) signaling regulates blood flow and pressure. *Hypertension* **70**, 426–434 (2017).

90. Akhter, M. Z. et al. Programming to S1PR1(+) endothelial cells promotes restoration of vascular integrity. *Circ. Res.* **129**, 221–236 (2021).

91. McGinley, M. P. & Cohen, J. A. Sphingosine 1-phosphate receptor modulators in multiple sclerosis and other conditions. *Lancet* **398**, 1184–1194 (2021).

92. Baweja, S. et al. Hepatopulmonary syndrome is associated with low sphingosine-1-phosphate levels and can be

ameliorated by the functional agonist fingolimod. *J. Hepatol.* **79**, 167–180 (2023).

93. Cromer, W. E., Mathis, J. M., Granger, D. N., Chaitanya, G. V. & Alexander, J. S. Role of the endothelium in inflammatory bowel diseases. *World J. Gastroenterol.* **17**, 578–593 (2011).

94. Dubsky, M. et al. Endothelial dysfunction in diabetes mellitus: New insights. *Int. J. Mol. Sci.* **24**, https://doi.org/10.3390/ijms241310705 (2023).

95. Anyfanti, P. et al. Endothelial dysfunction in psoriasis: An updated review. *Front. Med.* **9**, 864185 (2022).

96. Molema, G., Zijlstra, J. G., van Meurs, M. & Kamps, J. Renal microvascular endothelial cell responses in sepsis-induced acute kidney injury. *Nat. Rev. Nephrol.* **18**, 95–112 (2022).

97. Houston, S. Immunosuppression. *Nat. Immunol.* **23**, 1520 (2022).

98. Bernheim, O. et al. The management of immunosuppression in patients with inflammatory bowel disease and cancer. *Gut* **62**, 1523–1528 (2013).

99. Roberts, M. B. & Fishman, J. A. Immunosuppressive agents and infectious risk in transplantation: Managing the "Net State of Immunosuppression. *Clin. Infect. Dis.* **73**, e1302–e1317 (2021).

100. Blat, D., Zigmond, E., Alteber, Z., Waks, T. & Eshhar, Z. Suppression of murine colitis and its associated cancer by carcinoembryonic antigen-specific regulatory T cells. *Mol. Ther.* **22**, 1018–1028 (2014).

101. Becker, C., Fantini, M. C. & Neurath, M. F. High resolution colonoscopy in live mice. *Nat. Protoc.* **1**, 2900–2904 (2006).

102. Helms, M. N., Torres-Gonzalez, E., Goodson, P. & Rojas, M. Direct tracheal instillation of solutes into mouse lung. *J. Vis. Exp.* https://doi.org/10.3791/1941 (2010).

103. Liang, W. et al. Airway dysbiosis accelerates lung function decline in chronic obstructive pulmonary disease. *Cell Host Microbe* **31**, 1054–1070 e1059 (2023).

104. Elinav, E. et al. NLRP6 inflammasome regulates colonic microbial ecology and risk for colitis. *Cell* **145**, 745–757 (2011).

105. Cruz-Acuna, R. et al. Synthetic hydrogels for human intestinal organoid generation and colonic wound repair. *Nat. Cell Biol.* **19**, 1326–1335 (2017).

106. Yuan, Y. et al. Structures of signaling complexes of lipid receptors S1PR1 and S1PR5 reveal mechanisms of activation and drug recognition. *Cell Res.* **31**, 1263–1274 (2021).

107. Zhao, C. et al. Biased allosteric activation of ketone body receptor HCAR2 suppresses inflammation. *Mol. Cell* **83**, 3171–3187 (2023).

108. Zhao, J. et al. Prospect of acromegaly therapy: molecular mechanism of clinical drugs octreotide and paltusotine. *Nat. Commun.* **14**, 962 (2023).

109. Zheng, S. Q. et al. MotionCor2: anisotropic correction of beam-induced motion for improved cryo-electron microscopy. *Nat. Methods* **14**, 331–332 (2017).

110. Zhang, K. Gctf: Real-time CTF determination and correction. *J. Struct. Biol.* **193**, 1–12 (2016).

111. Kimanius, D., Dong, L., Sharov, G., Nakane, T. & Scheres, S. H. W. New tools for automated cryo-EM single-particle analysis in RELION-4.0. *Biochem. J.* **478**, 4169–4185 (2021).

112. Punjani, A., Rubinstein, J. L., Fleet, D. J. & Brubaker, M. A. cryoSPARC: algorithms for rapid unsupervised cryo-EM structure determination. *Nat. Methods* **14**, 290–296 (2017).

113. Pettersen, E. F. et al. UCSF ChimeraX: Structure visualization for researchers, educators, and developers. *Protein Sci.* **30**, 70–82 (2021).

114. Emsley, P., Lohkamp, B., Scott, W. G. & Cowtan, K. Features and development of Coot. *Acta Crystallogr. D. Biol. Crystallogr.* **66**, 486–501 (2010).

115. Liebschner, D. et al. Macromolecular structure determination using X-rays, neutrons and electrons: recent developments in Phenix. *Acta Crystallogr. D. Struct. Biol.* **75**, 861–877 (2019).

116. Jo, S., Kim, T., Iyer, V. G. & Im, W. CHARMM-GUI: a web-based graphical user interface for CHARMM. *J. Comput. Chem.* **29**, 1859–1865 (2008).

117. Lee, J. et al. CHARMM-GUI Input generator for NAMD, GROMACS, AMBER, OpenMM, and CHARMM/OpenMM simulations using the CHARMM36 additive force field. *J. Chem. Theory Comput.* **12**, 405–413 (2016).

118. Huang, J. et al. CHARMM36m: an improved force field for folded and intrinsically disordered proteins. *Nat. Methods* **14**, 71–73 (2017).

119. Pall, S. et al. Heterogeneous parallelization and acceleration of molecular dynamics simulations in GROMACS. *J. Chem. Phys.* **153**, 134110 (2020).

120. Xu, Z. et al. Ligand recognition and G-protein coupling of trace amine receptor TAAR1. *Nature* **624**, 672–681 (2023).

Author contributions

F.L., Z.S., W.Y., H.Zheng. and C.D. performed study concept, literature search, experimentation design, and critical revision of the manuscript. H.Zheng., L.G., Z.Z., Z.K., X.T., and Q.Z. performed in vivo and in vitro experimentation and analysis. Z.S., W.Y., and C.D. initiated the biased signaling of the S1PR1 project. J.Y., Z.X., J.Z., and X.T. prepared the cryo-EM grids, collected cryo-EM images, and performed map calculations. K.W. contributed to the G protein dissociation, β-arrestin recruitment, and internalization assays. X.T. carried out MD simulations. Manuscript drafting: H.Zheng., J.Y., and C.D. Intellectual contributions, manuscript editing and material support: H.W., Z.C., J.B., J.C., H.Zhang., W.L., F.L., Z.S., W.Y., and C.D.

Competing interests

The authors declare no competing interests.

Additional information

Supplementary information The online version contains supplementary material available at
https://doi.org/10.1038/s41467-025-57124-x.

Correspondence and requests for materials should be addressed to Wei Yan, Zhenhua Shao, Fengming Luo or Cheng Deng.

Peer review information *Nature Communications* thanks the anonymous reviewers for their contribution to the peer review of this work. A peer review file is available.

Reprints and permissions information is available at
http://www.nature.com/reprints

Publisher's note Springer Nature remains neutral with regard to jurisdictional claims in published maps and institutional affiliations.